

# BLR kinematics and Black Hole Mass in Markarian 6

V. T. Doroshenko,<sup>1,2,3\*</sup> S. G. Sergeev,<sup>1,3\*</sup> S. A. Klimanov,<sup>4</sup> V. I. Pronik,<sup>1,3</sup>  
 Yu. S. Efimov<sup>1†</sup>

<sup>1</sup>Crimean Astrophysical Observatory, P/O Nauchny Crimea 98409, Ukraine

<sup>2</sup>Crimean Laboratory of the Sternberg Astronomical Institute, P/O Nauchny, 98409 Crimea, Ukraine

<sup>3</sup>Isaac Newton Institute of Chile, Crimean Branch, Ukraine

<sup>4</sup>Central Astronomical Observatory of Pulkovo, Pulkovskoe Shosse 65, 196140 St. Petersburg, Russia

Accepted . Received ; in original form

## ABSTRACT

We present results of the optical spectral and photometric observations of the nucleus of Markarian 6 made with the 2.6-m Shajn telescope at the Crimean Astrophysical Observatory. The continuum and emission Balmer line intensities varied more than by a factor of two during 1992–2008. The lag between the continuum and H $\beta$  emission line flux variations is  $21.1 \pm 1.9$  days. For the H $\alpha$  line the lag is about 27 days but its uncertainty is much larger. We use Monte-Carlo simulation of the random time series to check the effect of our data sampling on the lag uncertainties and we compare our simulation results with those obtained by random subset selection (RSS) method of Peterson et al. (1998). The lag in the high-velocity wings are shorter than in the line core in accordance with the virial motions. However, the lag is slightly larger in the blue wing than in the red wing. This is a signature of the infall gas motion. Probably the BLR kinematic in the Mrk 6 nucleus is a combination of the Keplerian and infall motions. The velocity-delay dependence is similar for individual observational seasons. The measurements of the H $\beta$  line width in combination with the reverberation lag permits us to determine the black hole mass,  $M_{BH} = (1.8 \pm 0.2) \times 10^8 M_{\odot}$ . This result is consistent with the AGN scaling relationships between the BLR radius and the optical continuum luminosity ( $R_{BLR} \propto L^{0.5}$ ) as well as with the black-hole mass–luminosity relationship ( $M_{BH} - L$ ) under the Eddington luminosity ratio for Mrk 6 to be  $L_{bol}/L_{Edd} \sim 0.01$ .

**Key words:** galaxies: active – galaxies: nuclei – galaxies: Seyfert – galaxies: individual: Mrk 6

## 1 INTRODUCTION

Over the past nearly 30 years the method of reverberation mapping (RM) (Peterson 1988 and reference therein) has become one of the standard methods for studying the Active Galactic Nuclei (AGNs). It is based on the assumption that in a typical Seyfert galaxy the source of continuous radiation near a black hole, named as accretion disc (AD), is expected to be of order  $10^{13} - 10^{14}$  cm. Photoionization of the gas located at a distance of order  $10^{16}$  cm produces broad emission lines. The relationship between the continuum and emission line fluxes can be represented by the equation (Blandford & McKee 1982)

$$L(t) = \int \Psi(\tau)C(t - \tau)dt,$$

where  $C(t)$  and  $L(t)$  are the observed continuum and emission-line light curves, and  $\Psi(\tau)$  is the 1-d transfer function (TF). The TF determines the emission line response to a  $\delta$ -function continuum pulse as seen by a distant observer. So, the emission lines "echo" or "reverberate" in response to the continuum changes with a delay  $\tau$ . The size of the region where broad lines (BLR) are formed can be written as  $R_{BLR} = c\tau$ . The primary task of the RM method is to use the observable  $C(t)$  and  $L(t)$  to solve the above integral equation for the TF in order to obtain information about the geometry and physical conditions in the BLR. Unfortunately, it is very difficult to find a unique and reliable solution to this equation. However, it is possible to find a temporal shift (lag) between the continuum and emission line light curves using the cross-correlation analysis.

\* E-mail: vdorosh@sai.crimea.ua (VTD);

sergeev@crao.crimea.ua (SGS).

† Deceased, 2011 October 21.

Applying the virial assumption, the mass of the black hole can be determined when the BLR size and the velocity dispersion of the BLR gas are known (Peterson et al. 2004). The present tremendous progress being made in black hole mass estimates can be attributed to the reverberation method.

On the other hand, different segments of a single emission line seem to be formed at different effective distances from the ionizing source. In that case, the response in the flux of emission line at line-of-sight velocity  $V_r$  and time delay  $\tau$  is caused by the 2-d transfer function or "velocity delay map" (Horne et al. 2004). The reverberation technique applied to different parts of a single emission line allows one to make conclusions about the velocity field of the BLR gas. To the present time, considerable progress was made in understanding the direction of the BLR gas motion (Gaskell 2009; Bentz et al. 2008; Denney et al. 2009; Bentz et al. 2010). For example, some distinctive signatures for infalling gas motions in NGC 3516 and Arp 151 (Bentz et al. 2009b; Denney et al. 2009) were revealed: the blue side of the line lagging the red side. NGC 5548 shows the virialized gas motions with the symmetric lags on both the red and blue sides of line. However, the BLR gas in NGC 3227 shows the signature of radial outflow: shorter lags for the blue-shifted gas and longer lags for the red-shifted gas (Denney et al. 2009).

More than 40 AGNs have been studied by the RM up to now (Peterson et al. 2004; Bentz et al. 2009b; Denney et al. 2010). However, the Mrk 6 nucleus is absent in this list. Just a few studies of this galaxy have been made by the reverberation method. We can mention the paper by Doroshenko & Sergeev (2003) based on the archive spectra of Mrk 6 obtained from 1970–1991 using the image tube spectrograph at the 2.6-m telescope of the Crimean Astrophysical Observatory (CrAO). There is also another paper by Sergeev et al. (1999) that includes the results of the 1992–1997 observations with the same spectrograph but with a CCD detector. In this paper a lag in the flux variations of hydrogen lines with respect to the adjacent continuum flux variations was reported for the first time and changes in the line profiles were studied.

Mrk 6 is a Seyfert 1.5 galaxy (Sy 1.5). This galaxy was one of the first galaxies in which the strong variability of the  $H\beta$  emission line profile was detected by Khachikian & Weedman (1971). Although there have not been many optical observations of Mrk 6, there are some radio studies of Mrk 6 available (Kukula et al. 1996; Kharb et al. 2006), which revealed the complex structure of the radio emission. The X-ray emission from the Mrk 6 nucleus (Feldmeier et al. 1999; Malizia et al. 2003; Immler et al. 2003; Schurch et al. 2006) exhibits a complex X-ray absorption and some authors assume that the BLR is a possible location of this absorption complex (Malizia et al. 2003).

In this paper we present the results of our optical spectroscopic observations of Mrk 6 during the monitoring campaign from 1998 to 2008 performed after publishing our earlier papers with observations made from 1970–1997. For completeness we apply our analysis to all the spectral CCD observations that have been made since 1992 and we also use the results of our photometric observations in the  $V$  band. Throughout the entire work, we take  $z = 0.01865$  from our spectral estimates, the distance to Mrk 6 equal to

$D = 81$  Mpc, and  $H_0 = 70$   $\text{km s}^{-1} \text{Mpc}^{-1}$ . The observations and data reduction are described in Section 2. We present the cross-correlation analysis in Section 3, the line width measurements in Section 4; the estimates of the black hole mass, the mass–luminosity and lag–luminosity diagrams are presented in Sections 5 and 6, the velocity-resolved reverberation lag analysis is performed in Section 7. The results are summarized in Section 8.

## 2 OBSERVATIONS

### 2.1 Spectral observations and data processing

The  $H\alpha$  and  $H\beta$  spectra of the Seyfert galaxy Mrk 6 were obtained from the CrAO 2.6-m Shajn telescope. Prior to 2005 we used the Astro-550 CCD which had a size  $580 \times 520$  pixels and was cooled by liquid nitrogen. The dispersion was  $2.2 \text{ \AA pixel}^{-1}$ , and the spectral resolution was about  $7\text{--}8 \text{ \AA}$ . The working wavelength range was about  $1200 \text{ \AA}$ . The entrance slit width was  $3''$ . For technical reasons it was not always possible to set the same position angle (PA) of the entrance slit. Most of the observations were performed along  $\text{PA} \sim 125^\circ$  or  $\text{PA} \sim 90^\circ$ . The typical exposure time was about one hour. The "extraction window" was equal to  $11''$ .

In July 2005 the Astro-550 CCD was replaced with the SPEC-10  $1340 \times 100$  pixel CCD, thermoelectrically cooled up to  $-100^\circ\text{C}$ . In this case the dispersion was  $1.8 \text{ \AA pixel}^{-1}$ . A  $3''.0$  slit with a  $90^\circ$  position angle was utilized for these observations. The higher quantum efficiency (95% max.) and the lower read noise of this CCD allowed us to obtain higher quality spectra under shorter exposure times. The spectral wavelength range for these data sets was about  $2000 \text{ \AA}$  near the  $H\alpha$  and  $H\beta$  regions. However, the red and blue edges of the CCD frame are unusable because of vignetting. Generally, all spectra in both spectral regions were obtained with a single exposure during the whole night. Our final data set for 1998–2008 consists of 135 spectra in the  $H\beta$  region and 48 spectra in  $H\alpha$ . The mean signal-to-noise ratio (S/N) is equal to 32 for the Astro-550 and 73 for the SPEC-10 in the  $H\beta$  region and is equal to 40 and 66 in the  $H\alpha$  region, respectively.

As a rule, each observation was preceded by four short-time ( $\sim 10$  s) exposures of the standard star BS 3082, whose spectra were obtained at approximately the same zenith distance as that of the galaxy. The spectral energy distribution for these spectra was taken from Kharitonov et al. (1988). The standard star spectra were used to remove telluric absorption features from the spectra of Mrk 6, to provide the relative flux calibration, and to measure the seeing parameter defined as the FWHM of the cross-dispersion profile on the CCD image. The description of the primary data processing as well as some details of absolute calibration and measurements of the spectra are given in Sergeev et al. (1999).

The flux calibration was carried out by assuming the narrow emission line fluxes to be constant. We chose the narrow [OIII] $\lambda 5007$  (for the  $H\beta$  region) and [SII] $\lambda\lambda 6717, 6732$  emission lines (for the  $H\alpha$  region) as the internal flux standards. Their absolute fluxes were measured from the spectra obtained under photometric conditions by using the spectra of the comparison star BS 3082. The

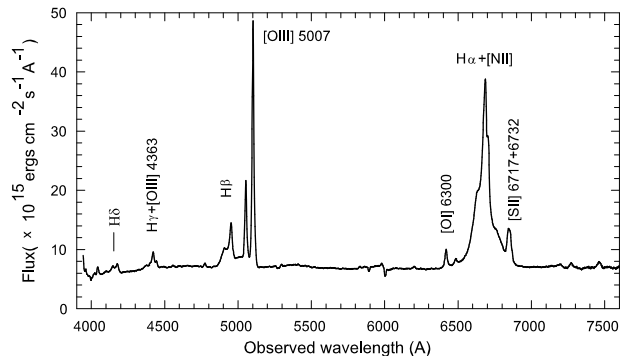


**Figure 1.** Mean Mrk 6 spectrum obtained by combining the quasi-simultaneous pairs of spectra from the  $H\alpha$  and  $H\beta$  spectral regions (SPEC-10 CCD only).

mean fluxes in these lines are given in Sergeev et al. (1999):  $F([\text{OIII}]\lambda 5007) = (6.90 \pm 0.11) \times 10^{-13} \text{ erg s}^{-1} \text{ cm}^{-2}$ ;  $F([\text{SII}]\lambda\lambda(6717 + 6731)) = (1.61 \pm 0.09) \times 10^{-13} \text{ erg s}^{-1} \text{ cm}^{-2}$ , and  $F([\text{OI}]\lambda 6300) = (0.597 \pm 0.035) \times 10^{-13} \text{ erg s}^{-1} \text{ cm}^{-2}$ . The  $[\text{SII}]$  lines reside on the far wings of the broad  $H\alpha$  line. Thus, to measure their fluxes, we selected the pseudo-continuum zones closely spaced around each line. The line fluxes were measured by integrating the spectra over the specified wavelength intervals and above the continuum (or local pseudo-continuum), which was fitted with a straight line in the selected zones. The mean continuum flux per unit wavelength was determined in two windows: at 5162–5186 Å (designated as  $F_{5170}$ ) and 6985–7069 Å (designated as  $F_{7030}$ ). The continuum zones and integration limits are the same as in Sergeev et al. (1999). The line and continuum flux uncertainties contain errors related to the S/N of the source spectra, atmospheric dispersion, changes in the position angle of the slit, and seeing effects. Evaluation of these uncertainties is considered in Sergeev et al. (1999). The mean spectrum of Mrk 6 produced by combining 23 quasi-simultaneous pairs of spectra from the  $H\alpha$  and  $H\beta$  regions is shown in Fig.1. Figure 2 shows the mean and rms spectra of Mrk 6 based on our observations in 1992–2008.

## 2.2 Optical photometry

In order to improve the time resolution of our data set in the  $F_{5170}$  continuum we added the  $V$ -band photometry to our spectral observations. Photometric data came from two sources: the  $UBV$  observations were made at the Crimean Laboratory of the Sternberg Astronomical Institute of Moscow University, and the  $BVRI$  observations were obtained at the CrAO. The  $UBV$  observations were obtained in the standard Johnson photometric system and were carried out from 1986 to 2009 at the 60-cm Zeiss telescope with a photo-multiplier detector through the aperture  $A=27''.5$ . The mean uncertainty of Mrk 6 in the  $V$ -band is  $0^m.022$ . These data were partially published by Doroshenko (2003).

In 2001 we started regular observations of Mrk 6 using the CrAO 70-cm AZT-8 telescope and the AP7p CCD. The CCD field covers  $15' \times 15'$ . Photometric fluxes were measured within an aperture of  $15''.0$ . The mean uncertainty of the

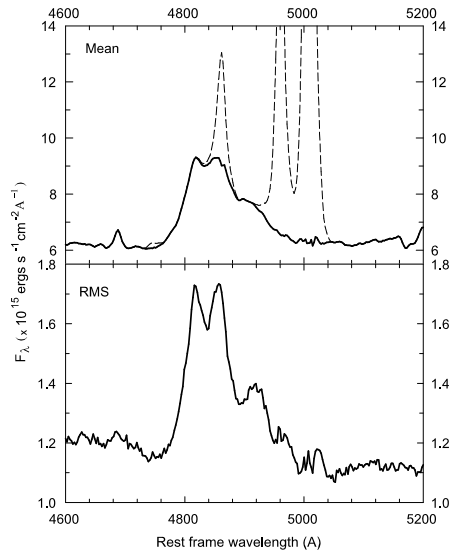


**Figure 2.** Mean and rms spectra of Mrk 6 in the  $H\beta$  region from our observations 1992–2008.

$V$ -band CCD observations is  $0^m.009$ . Further details about the instrumentation, reductions, and measurements of the  $BVRI$  photometric data can be found in Doroshenko et al. (2005). These data were partially published by Sergeev et al. (2005).

## 2.3 Light curves

Light curves in  $H\alpha$  and  $H\beta$ , and the adjacent continuum are shown in Fig. 3 for spectral observations corrected for seeing. The continuum light curves obtained from the photometric  $V$ -band observations were scaled to the flux density measured from the spectroscopic observations. To this end, we used the observations made on the same nights almost simultaneously. We have 29 appropriate observational nights at the 2.6-m and 70-cm telescopes (spectra plus CCD photometry) and 40 appropriate nights at the 2.6-m and 60-cm telescopes (spectra plus the  $UBV$  photoelectric photometry). The correlation coefficient between the spectral continuum and the  $V$ -band CCD flux for the appropriate nights is  $r=0.984$  ( $n=29$  points), and the correlation coefficient between the spectral continuum and the  $V$ -band flux from the  $UBV$  observations is  $r=0.993$  ( $n=40$  points). Using the regression equations, we converted our  $V$ -band photometric fluxes to the spectral continuum fluxes ( $F_{5170}$ ). For the nights where both spectral and photometric observations were available, the continuum fluxes are calculated as the weighted average. The fluxes were not corrected for the host starlight contamination and Galactic reddening.

**Tables 1 and 2 give the light curves from the spectral observations for 1998–2008 (the data for 1991–1997 are available in Sergeev et al. 1999). The  $H\beta$  and  $H\gamma$  line fluxes together with the spectral continuum fluxes  $F_{5170}$  are shown in Table 1. The  $H\alpha$  line fluxes and the spectral continuum fluxes  $F_{7030}$  are shown in Table 2. Table 3 gives combined continuum fluxes from both the spectral observations and from  $V$ -band photometric measurements for 1991–**

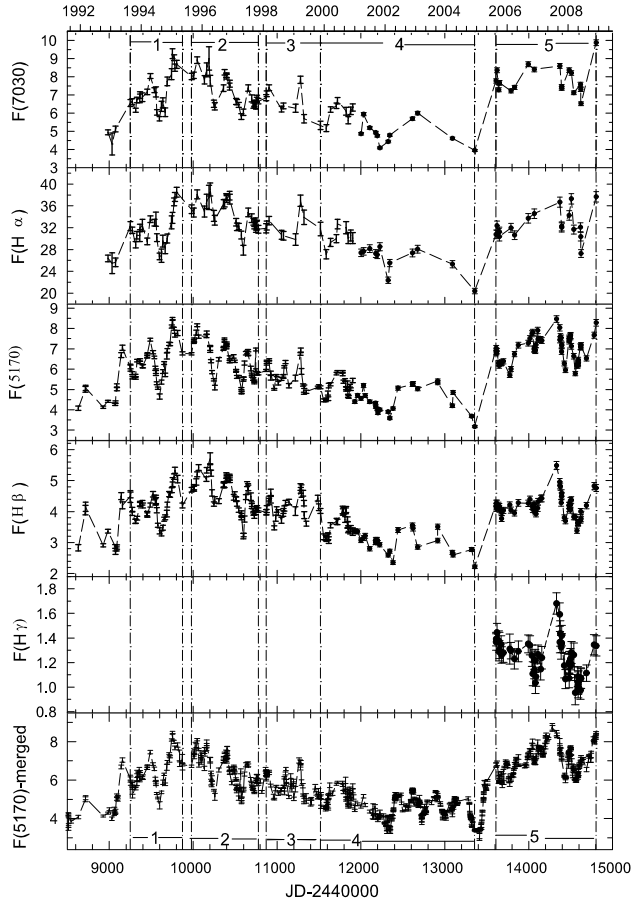


**Figure 3.** Light curves of Mrk 6 shown for the continua and  $H\alpha$ ,  $H\beta$ , and  $H\gamma$  lines. Narrow lines were not subtracted from the fluxes. Bottom panel shows the merged continuum light curve used for cross-correlation analysis. Units are  $10^{-13}$  erg  $\text{cm}^{-2}$   $\text{s}^{-1}$  and  $10^{-15}$  erg  $\text{cm}^{-2}$   $\text{s}^{-1}$   $\text{\AA}^{-1}$  for the lines and continua, respectively. The vertical dash-dotted lines show the boundaries of the five time intervals considered in the present paper.

**2008.** All the fluxes are seeing-corrected. These light curves have been used for the subsequent time-series analysis.

Bottom panel in Figure 3 shows the combined light curve from different telescopes. The combined light curve shows long time scale continuum variability in Mrk 6 as well as more rapid random changes. The flux maxima were observed in 1995–1996 and in 2007.

Statistical parameters of the light curves for the lines and continuum are listed in Table 4. Column 1 gives the spectral features; column 2 gives a number of data points; column 3 is the median time interval between the data points. The combined continuum light curve is sampled better than the  $H\beta$  light curve, the  $H\beta$  light curve is sampled better than  $H\alpha$ . The mean flux and standard deviation are given in columns 4 and 5, and column 6 lists the variance  $F_{var}$  calculated as the ratio of the rms fluctuation, corrected for the effect of measurement errors, to the mean flux.  $R_{max}$  in column 7 is the ratio between the maximum and minimum fluxes corrected for the measurement errors. Uncertainties in  $F_{var}$  and  $R_{max}$  were computed assuming that a light curve is a set of statistically dependent values, i.e., a random pro-

**Table 1.** F5170 spectral continuum, the  $H\beta$  and  $H\gamma$  line fluxes.

JD-2,440,000	F5170	$H\beta$	$H\gamma$
10869.449	$5.932 \pm 0.057$	$3.980 \pm 0.079$	–
10875.449	$6.279 \pm 0.087$	$3.987 \pm 0.093$	–
10876.379	$6.365 \pm 0.085$	$4.082 \pm 0.112$	–
10905.395	$6.451 \pm 0.057$	$4.420 \pm 0.080$	–
10906.273	$6.352 \pm 0.088$	$4.329 \pm 0.098$	–
10924.432	$5.684 \pm 0.079$	$4.511 \pm 0.085$	–
10966.379	$5.008 \pm 0.058$	$3.476 \pm 0.065$	–
10982.395	$5.570 \pm 0.101$	$3.792 \pm 0.096$	–
10994.387	$5.678 \pm 0.062$	$4.072 \pm 0.085$	–
11014.516	$5.302 \pm 0.091$	$3.971 \pm 0.094$	–
11052.563	$5.519 \pm 0.081$	$3.724 \pm 0.100$	–
11074.574	$5.665 \pm 0.064$	$3.939 \pm 0.086$	–
11076.516	$5.628 \pm 0.080$	$4.022 \pm 0.078$	–
11085.570	$6.117 \pm 0.066$	$4.102 \pm 0.087$	–
11100.512	$6.344 \pm 0.076$	$4.283 \pm 0.079$	–
11141.406	$5.155 \pm 0.087$	$4.316 \pm 0.087$	–
11218.281	$5.525 \pm 0.117$	$4.022 \pm 0.133$	–
11278.395	$6.743 \pm 0.074$	$4.795 \pm 0.103$	–
11281.383	$6.927 \pm 0.087$	$4.687 \pm 0.099$	–
11290.402	$5.878 \pm 0.187$	$4.668 \pm 0.201$	–
11310.289	$5.216 \pm 0.067$	$4.594 \pm 0.090$	–
11319.313	$4.817 \pm 0.063$	$4.276 \pm 0.086$	–
11322.305	$5.134 \pm 0.148$	$3.885 \pm 0.113$	–
11349.324	$4.884 \pm 0.084$	$3.615 \pm 0.078$	–
11485.504	$5.096 \pm 0.072$	$4.438 \pm 0.089$	–
11497.434	$5.160 \pm 0.086$	$4.141 \pm 0.113$	–
11516.551	$5.103 \pm 0.073$	$4.020 \pm 0.078$	–
11557.418	$4.465 \pm 0.077$	$3.188 \pm 0.098$	–
11577.406	$4.456 \pm 0.066$	$3.151 \pm 0.087$	–
11587.293	$4.514 \pm 0.070$	$3.119 \pm 0.079$	–
11606.383	$4.821 \pm 0.112$	$3.192 \pm 0.127$	–
11608.285	$4.540 \pm 0.089$	$3.187 \pm 0.094$	–
11615.340	$5.173 \pm 0.114$	$3.081 \pm 0.108$	–
11636.270	$5.252 \pm 0.076$	$3.561 \pm 0.084$	–
11707.402	$5.783 \pm 0.095$	$3.687 \pm 0.092$	–
11720.336	$5.875 \pm 0.069$	$3.671 \pm 0.087$	–
11780.555	$5.757 \pm 0.102$	$4.052 \pm 0.123$	–
11782.555	$5.868 \pm 0.080$	$3.989 \pm 0.101$	–
11791.531	$5.385 \pm 0.093$	$4.017 \pm 0.126$	–
11810.531	$5.463 \pm 0.075$	$3.751 \pm 0.097$	–
11821.582	$5.010 \pm 0.092$	$4.032 \pm 0.094$	–
11823.496	$5.049 \pm 0.072$	$4.068 \pm 0.097$	–
11838.508	$5.234 \pm 0.183$	$3.741 \pm 0.181$	–
11840.539	$5.027 \pm 0.103$	$3.574 \pm 0.111$	–
11844.496	$4.679 \pm 0.072$	$3.577 \pm 0.098$	–
11847.473	$4.688 \pm 0.089$	$3.433 \pm 0.116$	–
11853.582	$4.628 \pm 0.067$	$3.456 \pm 0.089$	–
11869.496	$5.184 \pm 0.073$	$3.363 \pm 0.082$	–
11878.449	$5.012 \pm 0.080$	$3.450 \pm 0.102$	–
11901.316	$5.436 \pm 0.106$	$3.354 \pm 0.123$	–
11926.270	$4.391 \pm 0.084$	$3.374 \pm 0.080$	–
11959.227	$4.689 \pm 0.129$	$3.360 \pm 0.151$	–
11999.270	$4.517 \pm 0.112$	$3.077 \pm 0.103$	–
12030.422	$5.191 \pm 0.100$	$3.149 \pm 0.105$	–
12050.465	$4.689 \pm 0.087$	$3.219 \pm 0.081$	–
12104.316	$4.394 \pm 0.069$	$2.805 \pm 0.079$	–
12174.539	$4.327 \pm 0.069$	$3.007 \pm 0.087$	–
12175.531	$4.153 \pm 0.084$	$3.094 \pm 0.087$	–
12192.551	$4.046 \pm 0.095$	$3.099 \pm 0.104$	–
12201.598	$3.845 \pm 0.105$	$2.994 \pm 0.133$	–
12223.543	$4.004 \pm 0.085$	$2.934 \pm 0.107$	–
12323.375	$3.899 \pm 0.054$	$2.424 \pm 0.063$	–
12343.473	$3.573 \pm 0.107$	$2.723 \pm 0.118$	–

**Table 1** – *continued* F5170 spectral continuum, the H $\beta$  and H $\gamma$  line fluxes.

JD-2,440,000	F5170	H $\beta$	H $\gamma$
12381.262	4.039 $\pm$ 0.125	2.356 $\pm$ 0.130	–
12441.359	5.067 $\pm$ 0.078	3.406 $\pm$ 0.082	–
12613.543	5.260 $\pm$ 0.085	3.500 $\pm$ 0.099	–
12619.543	5.285 $\pm$ 0.063	3.457 $\pm$ 0.075	–
12675.410	5.032 $\pm$ 0.106	2.854 $\pm$ 0.126	–
12914.605	5.412 $\pm$ 0.152	3.171 $\pm$ 0.156	–
12915.531	5.223 $\pm$ 0.067	3.445 $\pm$ 0.092	–
13089.324	4.197 $\pm$ 0.062	2.682 $\pm$ 0.066	–
13097.301	4.849 $\pm$ 0.205	2.603 $\pm$ 0.111	–
13319.496	3.639 $\pm$ 0.065	2.741 $\pm$ 0.055	–
13356.555	3.175 $\pm$ 0.060	2.219 $\pm$ 0.068	–
13611.563	6.791 $\pm$ 0.081	4.125 $\pm$ 0.075	1.342 $\pm$ 0.057
13612.553	6.812 $\pm$ 0.062	4.135 $\pm$ 0.058	1.368 $\pm$ 0.046
13621.523	6.877 $\pm$ 0.082	4.264 $\pm$ 0.079	1.417 $\pm$ 0.064
13641.566	6.279 $\pm$ 0.096	4.197 $\pm$ 0.078	1.347 $\pm$ 0.069
13647.570	6.158 $\pm$ 0.095	4.157 $\pm$ 0.075	1.260 $\pm$ 0.062
13648.594	6.310 $\pm$ 0.084	4.156 $\pm$ 0.077	1.332 $\pm$ 0.069
13649.559	6.276 $\pm$ 0.081	4.082 $\pm$ 0.073	1.277 $\pm$ 0.063
13670.555	6.284 $\pm$ 0.083	4.020 $\pm$ 0.068	1.317 $\pm$ 0.060
13676.583	6.309 $\pm$ 0.079	3.914 $\pm$ 0.065	1.235 $\pm$ 0.055
13698.469	6.366 $\pm$ 0.103	4.038 $\pm$ 0.081	1.255 $\pm$ 0.067
13774.453	5.677 $\pm$ 0.189	4.203 $\pm$ 0.114	1.290 $\pm$ 0.104
13788.344	5.997 $\pm$ 0.091	4.044 $\pm$ 0.067	1.269 $\pm$ 0.058
13830.238	6.715 $\pm$ 0.113	3.949 $\pm$ 0.086	1.206 $\pm$ 0.070
13875.332	7.178 $\pm$ 0.086	4.282 $\pm$ 0.086	1.264 $\pm$ 0.071
13994.566	7.272 $\pm$ 0.080	4.269 $\pm$ 0.077	1.326 $\pm$ 0.062
14013.613	7.496 $\pm$ 0.089	4.407 $\pm$ 0.087	1.317 $\pm$ 0.066
14038.555	7.741 $\pm$ 0.089	4.177 $\pm$ 0.086	1.227 $\pm$ 0.073
14048.566	7.806 $\pm$ 0.136	4.069 $\pm$ 0.100	1.085 $\pm$ 0.082
14064.551	7.001 $\pm$ 0.085	4.244 $\pm$ 0.081	1.116 $\pm$ 0.057
14065.617	6.963 $\pm$ 0.079	4.139 $\pm$ 0.075	1.195 $\pm$ 0.063
14076.461	6.903 $\pm$ 0.156	4.044 $\pm$ 0.082	1.194 $\pm$ 0.076
14078.551	6.923 $\pm$ 0.101	3.989 $\pm$ 0.090	1.015 $\pm$ 0.072
14086.559	7.182 $\pm$ 0.097	3.924 $\pm$ 0.080	1.062 $\pm$ 0.065
14106.531	7.897 $\pm$ 0.243	4.107 $\pm$ 0.186	–
14111.473	7.469 $\pm$ 0.079	4.316 $\pm$ 0.078	1.241 $\pm$ 0.064
14142.594	7.459 $\pm$ 0.097	4.418 $\pm$ 0.090	1.120 $\pm$ 0.074
14156.270	7.366 $\pm$ 0.132	4.429 $\pm$ 0.102	1.220 $\pm$ 0.077
14331.543	8.416 $\pm$ 0.086	5.376 $\pm$ 0.095	1.647 $\pm$ 0.073
14369.516	7.978 $\pm$ 0.124	4.843 $\pm$ 0.094	1.556 $\pm$ 0.081
14370.539	7.390 $\pm$ 0.197	4.736 $\pm$ 0.093	1.335 $\pm$ 0.074
14377.582	7.570 $\pm$ 0.110	4.714 $\pm$ 0.107	1.410 $\pm$ 0.088
14386.457	7.490 $\pm$ 0.098	4.184 $\pm$ 0.097	1.294 $\pm$ 0.082
14391.551	6.816 $\pm$ 0.097	4.384 $\pm$ 0.076	1.327 $\pm$ 0.061
14392.539	7.115 $\pm$ 0.097	4.410 $\pm$ 0.081	1.331 $\pm$ 0.066
14393.504	7.178 $\pm$ 0.093	4.517 $\pm$ 0.092	1.396 $\pm$ 0.071
14423.559	6.261 $\pm$ 0.101	3.715 $\pm$ 0.088	1.149 $\pm$ 0.084
14438.438	5.934 $\pm$ 0.100	3.612 $\pm$ 0.075	1.043 $\pm$ 0.066
14480.414	7.435 $\pm$ 0.082	4.110 $\pm$ 0.080	1.166 $\pm$ 0.067
14481.398	7.342 $\pm$ 0.086	4.108 $\pm$ 0.083	1.049 $\pm$ 0.065
14482.434	7.498 $\pm$ 0.091	4.016 $\pm$ 0.086	1.179 $\pm$ 0.075
14496.367	7.517 $\pm$ 0.114	4.244 $\pm$ 0.094	1.209 $\pm$ 0.074
14497.418	7.561 $\pm$ 0.123	3.955 $\pm$ 0.099	1.155 $\pm$ 0.082
14499.328	7.615 $\pm$ 0.090	4.125 $\pm$ 0.088	1.168 $\pm$ 0.077
14508.418	7.071 $\pm$ 0.106	4.272 $\pm$ 0.088	1.258 $\pm$ 0.076
14537.340	6.605 $\pm$ 0.099	3.742 $\pm$ 0.086	1.233 $\pm$ 0.082
14554.324	5.749 $\pm$ 0.125	3.736 $\pm$ 0.099	0.942 $\pm$ 0.083
14574.309	6.132 $\pm$ 0.269	3.303 $\pm$ 0.226	–
14586.309	6.284 $\pm$ 0.086	3.550 $\pm$ 0.074	1.064 $\pm$ 0.069
14587.281	6.184 $\pm$ 0.092	3.576 $\pm$ 0.080	1.003 $\pm$ 0.067
14588.266	6.264 $\pm$ 0.098	3.577 $\pm$ 0.082	1.027 $\pm$ 0.068
14590.309	6.278 $\pm$ 0.098	3.543 $\pm$ 0.076	0.968 $\pm$ 0.060

**Table 1** – *continued* F5170 spectral continuum, the H $\beta$  and H $\gamma$  line fluxes.

JD-2,440,000	F5170	H $\beta$	H $\gamma$
14591.273	6.440 $\pm$ 0.108	3.556 $\pm$ 0.086	1.020 $\pm$ 0.077
14617.344	7.076 $\pm$ 0.086	3.632 $\pm$ 0.081	0.955 $\pm$ 0.062
14620.301	7.053 $\pm$ 0.091	3.923 $\pm$ 0.090	1.053 $\pm$ 0.071
14622.426	7.141 $\pm$ 0.087	3.682 $\pm$ 0.084	1.048 $\pm$ 0.068
14687.547	6.498 $\pm$ 0.095	4.099 $\pm$ 0.073	1.091 $\pm$ 0.057
14779.629	7.584 $\pm$ 0.127	4.711 $\pm$ 0.106	1.328 $\pm$ 0.070
14804.566	8.214 $\pm$ 0.093	4.650 $\pm$ 0.086	1.305 $\pm$ 0.070

Units are  $10^{-13}$  ergs  $\text{cm}^{-2}$   $\text{s}^{-1}$  and  $10^{-15}$  ergs  $\text{cm}^{-2}$   $\text{s}^{-1}$   $\text{\AA}^{-1}$  for the lines and continuum, respectively.

cess. The  $F_{var}$  values in Table 4 are the lowest limits of actual  $F_{var}$  because the observed fluxes were not corrected for starlight contamination.

### 3 CROSS-CORRELATION BETWEEN THE CONTINUUM AND THE INTEGRAL BALMER LINE FLUX VARIATIONS

As mentioned in the Introduction, estimating the light travel time delay between the continuum and emission line flux variations is of special relevance for the determination of the BLR size, which, in turn, can be used for black hole mass measurements (see Wandel et al. 1999; Peterson et al. 2004). This time delay (or lag) is estimated through the cross-correlation function (CCF). Koratkar & Gaskell (1991) demonstrated that the CCF centroid gives the luminosity-weighted radius, in contrast to the CCF peak, which is more influenced by gas at small radii, according to Gaskell & Sparke (1986).

The time delays were computed using the interpolated cross-correlation function (ICCF) (Gaskell & Sparke 1986; White & Peterson 1994; Peterson 2001). We computed both the lag related to the CCF peak ( $\tau_{pk}$ ) and the CCF centroid ( $\tau_{cn}$ ). The CCF centroid was adopted to be measured above the correlation level at  $r \geq 0.8r_{max}$ . The lag uncertainties were computed using the model-independent Monte Carlo flux randomization/random subset selection (FR/RSS) technique described by Peterson et al. (1998). The number of realizations was as large as 4000. The uncertainties were computed from the distribution function for  $\tau_{pk}$  and  $\tau_{cn}$  at the 68% confidence, which corresponds to  $\pm 1\sigma$  errors for the normal distribution.

The spectra for the 1992 season were obtained with the 2'' entrance slit and they were discarded from the CCF analysis in order to exclude the aperture effects. The results of the cross-correlation analysis for the 1993–2008 interval are presented in Table 5. The meaning of symbols "s" and "scp" in the first and second columns of Table 5 is the same as in Table 4: "s" – from spectral observations only and "scp" – from combined spectral and photometric observations ("c" – CCD, "p" – photoelectric).

Figure 4 shows the cross-correlation results for the H $\beta$  and H $\alpha$  line fluxes with the continuum as well as autocorrelation functions of the continuum for the 1993–2008 time interval. Table 5 gives the cross-correlation results. When the continuum light curve is a combination of the spectral

**Table 2.** F7030 spectral continuum and H $\alpha$  fluxes.

JD-2,440,000	F7030	H $\alpha$
10869.359	6.858 $\pm$ 0.194	31.959 $\pm$ 0.796
10876.453	7.063 $\pm$ 0.177	32.400 $\pm$ 0.833
10905.332	7.403 $\pm$ 0.176	33.322 $\pm$ 0.722
11053.559	6.227 $\pm$ 0.177	30.750 $\pm$ 0.726
11075.582	6.408 $\pm$ 0.171	30.532 $\pm$ 0.713
11220.219	6.271 $\pm$ 0.231	29.815 $\pm$ 1.056
11279.324	7.851 $\pm$ 0.210	37.009 $\pm$ 0.962
11321.301	5.697 $\pm$ 0.265	33.947 $\pm$ 1.258
11517.488	5.327 $\pm$ 0.268	31.821 $\pm$ 1.134
11587.355	5.174 $\pm$ 0.195	27.152 $\pm$ 0.741
11638.250	6.202 $\pm$ 0.163	29.285 $\pm$ 0.743
11707.344	6.400 $\pm$ 0.165	30.001 $\pm$ 0.712
11721.324	6.689 $\pm$ 0.188	32.688 $\pm$ 0.838
11823.543	6.115 $\pm$ 0.221	32.067 $\pm$ 0.951
11847.531	5.611 $\pm$ 0.204	30.121 $\pm$ 0.891
11878.512	6.134 $\pm$ 0.216	30.642 $\pm$ 0.918
11902.461	6.325 $\pm$ 0.219	30.126 $\pm$ 0.899
12000.254	4.590 $\pm$ 0.381	28.123 $\pm$ 1.239
12031.402	6.159 $\pm$ 0.277	27.928 $\pm$ 1.015
12105.324	5.290 $\pm$ 0.183	28.077 $\pm$ 0.731
12176.520	4.917 $\pm$ 0.209	27.194 $\pm$ 0.780
12193.508	4.927 $\pm$ 0.263	28.147 $\pm$ 1.009
12225.438	3.968 $\pm$ 0.598	28.053 $\pm$ 1.987
12323.457	4.401 $\pm$ 0.166	22.116 $\pm$ 0.518
12343.551	4.813 $\pm$ 0.394	25.054 $\pm$ 1.615
12613.594	5.715 $\pm$ 0.277	26.821 $\pm$ 1.083
12675.477	5.779 $\pm$ 0.193	26.451 $\pm$ 0.827
13090.277	4.505 $\pm$ 0.297	24.783 $\pm$ 0.909
13356.465	3.857 $\pm$ 0.159	20.999 $\pm$ 0.656
13610.559	8.018 $\pm$ 0.215	31.853 $\pm$ 0.796
13621.555	8.487 $\pm$ 0.240	32.350 $\pm$ 0.891
13642.594	7.377 $\pm$ 0.235	31.616 $\pm$ 1.047
13648.551	7.688 $\pm$ 0.277	30.374 $\pm$ 1.081
13648.563	7.474 $\pm$ 0.218	30.213 $\pm$ 0.859
13789.316	7.176 $\pm$ 0.227	32.545 $\pm$ 0.986
13831.234	7.418 $\pm$ 0.186	30.618 $\pm$ 0.825
13994.586	8.940 $\pm$ 0.228	34.663 $\pm$ 0.875
14066.457	8.472 $\pm$ 0.257	34.872 $\pm$ 1.008
14370.563	8.707 $\pm$ 0.264	37.536 $\pm$ 1.117
14392.563	8.377 $\pm$ 0.206	36.161 $\pm$ 0.988
14393.527	8.125 $\pm$ 0.256	35.540 $\pm$ 1.017
14481.387	8.255 $\pm$ 0.243	34.970 $\pm$ 1.044
14508.445	8.117 $\pm$ 0.377	36.963 $\pm$ 1.866
14617.324	7.455 $\pm$ 0.205	31.689 $\pm$ 0.795
14620.316	8.052 $\pm$ 0.228	33.558 $\pm$ 0.900
14622.367	7.785 $\pm$ 0.204	32.227 $\pm$ 0.890
14804.543	10.004 $\pm$ 0.242	38.158 $\pm$ 0.965

Units are  $10^{-13}$  ergs cm $^{-2}$  s $^{-1}$  and  $10^{-15}$  ergs cm $^{-2}$  s $^{-1}$   $\text{\AA}^{-1}$  for the H $\alpha$  line and continuum, respectively.

and the photometric data (designated as *F5170scp* in Table 5) then the CCF computation has been carried out with the rebinning the *F5170scp* light curve to the times of observations of the first time series. This is because the combined continuum light curve has much more data points than the continuum light curves which consist from the spectral data only (designated as *F5170s* in Table 5). For the *F5170s* light curve, we follow a standard method of the CCF computation with rebinning both time series.

The variations of the H $\alpha$  and H $\beta$  fluxes are tightly correlated as well as variations of the continuum fluxes near both

**Table 3.** Combined F5170 continuum fluxes from spectral and photometric observations.

JD-2,440,000	F5170	Julian Date	F5170
8630.5781	4.072 $\pm$ 0.107	9783.2969	7.666 $\pm$ 0.098
8716.4258	5.003 $\pm$ 0.143	9814.2656	7.775 $\pm$ 0.124
8717.3633	5.083 $\pm$ 0.129	9838.3027	7.282 $\pm$ 0.356
8927.5117	4.125 $\pm$ 0.054	9839.3398	6.827 $\pm$ 0.240
8983.4009	4.277 $\pm$ 0.050	9867.3389	7.121 $\pm$ 0.303
9001.2852	4.483 $\pm$ 0.151	9871.3545	6.683 $\pm$ 0.252
9031.2314	3.991 $\pm$ 0.150	9872.3594	6.775 $\pm$ 0.080
9057.2441	4.225 $\pm$ 0.146	9980.5746	6.749 $\pm$ 0.058
9059.3291	4.483 $\pm$ 0.171	10008.5636	7.303 $\pm$ 0.052
9062.3330	4.331 $\pm$ 0.161	10009.5860	7.380 $\pm$ 0.072
9070.2891	4.274 $\pm$ 0.068	10010.5900	7.445 $\pm$ 0.083
9074.3203	4.378 $\pm$ 0.059	10013.5390	7.236 $\pm$ 0.251
9088.2656	5.198 $\pm$ 0.076	10015.5170	7.458 $\pm$ 0.255
9089.2578	5.019 $\pm$ 0.079	10024.5360	7.791 $\pm$ 0.289
9100.2910	5.021 $\pm$ 0.186	10036.5900	7.798 $\pm$ 0.119
9101.2930	5.116 $\pm$ 0.174	10047.5526	8.101 $\pm$ 0.057
9141.3047	6.684 $\pm$ 0.119	10064.5120	7.593 $\pm$ 0.072
9156.3203	7.048 $\pm$ 0.126	10069.4550	6.782 $\pm$ 0.231
9250.5977	6.075 $\pm$ 0.170	10092.2260	7.053 $\pm$ 0.241
9252.5757	6.082 $\pm$ 0.093	10094.2990	7.399 $\pm$ 0.253
9255.4814	5.841 $\pm$ 0.210	10096.3280	6.939 $\pm$ 0.234
9272.6016	5.799 $\pm$ 0.068	10102.3720	7.282 $\pm$ 0.255
9273.4551	5.769 $\pm$ 0.211	10133.2640	6.606 $\pm$ 0.229
9274.5796	5.568 $\pm$ 0.047	10135.3040	7.540 $\pm$ 0.276
9275.4990	5.164 $\pm$ 0.184	10139.4580	7.376 $\pm$ 0.252
9311.5742	5.665 $\pm$ 0.077	10156.3134	7.602 $\pm$ 0.067
9313.4385	5.567 $\pm$ 0.061	10159.3190	7.949 $\pm$ 0.275
9329.4219	5.841 $\pm$ 0.214	10161.4450	7.790 $\pm$ 0.082
9331.4531	6.418 $\pm$ 0.068	10201.5550	6.994 $\pm$ 0.165
9332.4521	6.027 $\pm$ 0.212	10202.4060	7.008 $\pm$ 0.092
9341.3809	6.313 $\pm$ 0.219	10212.2930	5.893 $\pm$ 0.229
9357.3135	6.540 $\pm$ 0.233	10213.4450	6.383 $\pm$ 0.078
9359.3467	6.090 $\pm$ 0.211	10218.3130	5.790 $\pm$ 0.225
9362.3525	6.017 $\pm$ 0.208	10222.3060	6.101 $\pm$ 0.223
9364.3281	6.334 $\pm$ 0.067	10225.3320	5.847 $\pm$ 0.077
9365.4180	6.448 $\pm$ 0.060	10246.3710	5.474 $\pm$ 0.060
9395.3750	6.140 $\pm$ 0.068	10258.3980	5.091 $\pm$ 0.110
9399.3984	6.155 $\pm$ 0.088	10304.4220	6.479 $\pm$ 0.081
9450.3438	6.618 $\pm$ 0.062	10361.5310	6.989 $\pm$ 0.068
9452.2461	6.651 $\pm$ 0.100	10363.4840	7.053 $\pm$ 0.070
9454.2734	6.731 $\pm$ 0.077	10364.5410	7.064 $\pm$ 0.274
9488.3398	7.461 $\pm$ 0.072	10372.4804	7.427 $\pm$ 0.040
9520.3281	6.829 $\pm$ 0.076	10392.5060	7.411 $\pm$ 0.271
9536.3867	6.575 $\pm$ 0.064	10395.4687	7.013 $\pm$ 0.049
9548.5000	6.048 $\pm$ 0.099	10396.4610	7.103 $\pm$ 0.063
9554.5234	5.900 $\pm$ 0.111	10397.4610	7.274 $\pm$ 0.063
9555.5117	5.813 $\pm$ 0.124	10399.4490	7.179 $\pm$ 0.078
9566.4570	5.304 $\pm$ 0.068	10401.4600	7.018 $\pm$ 0.246
9578.3984	5.070 $\pm$ 0.058	10403.4010	7.599 $\pm$ 0.267
9599.3672	4.653 $\pm$ 0.134	10404.4920	7.635 $\pm$ 0.258
9622.2734	5.361 $\pm$ 0.094	10406.5080	7.446 $\pm$ 0.240
9639.5547	5.878 $\pm$ 0.096	10408.5900	7.202 $\pm$ 0.229
9653.5635	6.298 $\pm$ 0.074	10430.3770	6.573 $\pm$ 0.224
9665.5331	5.784 $\pm$ 0.069	10434.3200	6.386 $\pm$ 0.055
9685.3984	6.646 $\pm$ 0.147	10435.3240	6.586 $\pm$ 0.072
9691.5078	6.915 $\pm$ 0.086	10436.4100	6.371 $\pm$ 0.052
9713.4539	7.374 $\pm$ 0.052	10461.5560	5.841 $\pm$ 0.195
9716.5488	7.064 $\pm$ 0.252	10482.5040	6.621 $\pm$ 0.088
9723.4297	7.226 $\pm$ 0.081	10483.4790	6.683 $\pm$ 0.220
9744.3984	8.089 $\pm$ 0.078	10484.4480	6.628 $\pm$ 0.209
9753.3086	8.467 $\pm$ 0.074	10487.3660	6.410 $\pm$ 0.213
9754.3789	8.249 $\pm$ 0.183	10491.4380	6.573 $\pm$ 0.222

**Table 3** – *continued* Combined F5170 continuum fluxes from spectral and photometric observations.

JD-2,440,000	F5170	Julian Date	F5170
9771.3086	7.988 ± 0.071	10495.3670	6.383 ± 0.057
10509.3810	6.054 ± 0.062	11085.5700	6.117 ± 0.066
10510.4262	5.990 ± 0.044	11088.4720	5.330 ± 0.184
10511.3540	5.608 ± 0.196	11100.5120	6.344 ± 0.076
10518.4320	5.408 ± 0.176	11105.5480	6.584 ± 0.214
10519.4260	5.638 ± 0.190	11110.5780	5.790 ± 0.195
10521.3830	5.709 ± 0.192	11111.5760	5.924 ± 0.207
10522.3851	5.517 ± 0.067	11141.4334	5.127 ± 0.081
10541.3549	5.524 ± 0.046	11163.4850	5.729 ± 0.185
10543.2960	5.059 ± 0.188	11164.3130	6.207 ± 0.220
10566.3030	6.464 ± 0.230	11176.5790	5.478 ± 0.192
10569.3380	5.517 ± 0.196	11192.3790	5.810 ± 0.201
10574.3634	5.080 ± 0.038	11197.2630	5.934 ± 0.211
10575.3160	4.840 ± 0.054	11199.3480	5.021 ± 0.174
10576.3520	4.868 ± 0.058	11218.2810	5.525 ± 0.117
10580.3820	5.252 ± 0.210	11261.4920	7.018 ± 0.250
10597.3852	5.460 ± 0.083	11274.3120	6.951 ± 0.229
10601.3550	5.540 ± 0.064	11278.3950	6.743 ± 0.074
10611.3440	6.296 ± 0.099	11279.2870	6.650 ± 0.237
10628.3590	6.778 ± 0.081	11281.3662	6.943 ± 0.081
10642.3320	6.824 ± 0.068	11290.4020	5.878 ± 0.187
10654.3320	6.808 ± 0.153	11306.3890	5.709 ± 0.203
10655.3280	6.764 ± 0.081	11310.2890	5.216 ± 0.067
10687.5700	6.033 ± 0.116	11319.3130	4.817 ± 0.063
10697.4208	5.833 ± 0.048	11322.3050	5.134 ± 0.148
10699.5270	5.661 ± 0.057	11346.3850	5.164 ± 0.203
10705.5590	5.587 ± 0.188	11349.3240	4.884 ± 0.084
10714.5080	5.504 ± 0.063	11400.5350	4.851 ± 0.247
10715.5200	5.526 ± 0.061	11407.5290	5.021 ± 0.167
10728.5390	5.333 ± 0.052	11409.5370	4.841 ± 0.191
10729.5080	5.399 ± 0.056	11454.5560	5.658 ± 0.207
10747.5430	5.962 ± 0.076	11467.4890	5.310 ± 0.181
10748.4650	5.950 ± 0.057	11485.5040	5.096 ± 0.072
10755.5340	6.196 ± 0.211	11488.6040	5.136 ± 0.193
10758.5249	5.924 ± 0.052	11493.3450	5.438 ± 0.202
10759.4380	5.777 ± 0.076	11497.4340	5.160 ± 0.086
10760.5280	5.924 ± 0.195	11516.5510	5.103 ± 0.073
10761.5130	6.185 ± 0.206	11522.5520	4.610 ± 0.162
10762.5670	6.196 ± 0.209	11524.5720	5.184 ± 0.231
10777.4300	5.776 ± 0.067	11525.4560	5.126 ± 0.190
10801.2660	5.955 ± 0.203	11557.3624	4.581 ± 0.056
10817.3570	5.389 ± 0.177	11577.4060	4.456 ± 0.066
10863.3710	6.562 ± 0.221	11581.3890	4.547 ± 0.153
10866.3790	6.377 ± 0.234	11586.4480	4.601 ± 0.157
10867.4230	6.291 ± 0.210	11587.3295	4.542 ± 0.053
10868.4180	6.453 ± 0.212	11588.5210	4.907 ± 0.163
10869.4520	5.996 ± 0.047	11598.2560	4.721 ± 0.180
10873.4040	6.410 ± 0.208	11603.2890	4.879 ± 0.192
10874.2920	6.324 ± 0.228	11605.4510	5.145 ± 0.191
10875.4490	6.279 ± 0.209	11606.3830	4.821 ± 0.112
10876.3961	6.207 ± 0.063	11608.3236	4.493 ± 0.056
10905.3950	6.451 ± 0.057	11612.3560	5.097 ± 0.181
10906.2730	6.352 ± 0.088	11615.3400	5.173 ± 0.114
10924.4482	5.708 ± 0.074	11628.3200	5.729 ± 0.209
10957.3660	5.136 ± 0.200	11636.2700	5.252 ± 0.076
10966.3790	5.008 ± 0.058	11661.2870	5.310 ± 0.194
10982.3950	5.570 ± 0.101	11707.4020	5.783 ± 0.095
10994.3922	5.671 ± 0.053	11720.3360	5.875 ± 0.069
11014.5160	5.302 ± 0.091	11780.5550	5.757 ± 0.102
11044.3860	5.408 ± 0.220	11782.5550	5.868 ± 0.080
11050.5250	5.498 ± 0.181	11788.5360	5.638 ± 0.243
11052.5630	5.519 ± 0.081	11791.5310	5.385 ± 0.093

**Table 3** – *continued* Combined F5170 continuum fluxes from spectral and photometric observations.

JD-2,440,000	F5170	Julian Date	F5170
11074.5740	5.665 ± 0.064	11810.5310	5.463 ± 0.075
11076.4995	5.650 ± 0.077	11817.5320	5.986 ± 0.243
11818.5550	5.408 ± 0.185	12349.3890	3.483 ± 0.133
11821.5820	5.010 ± 0.092	12366.2620	3.890 ± 0.024
11823.4960	5.049 ± 0.072	12367.2780	3.984 ± 0.026
11838.5080	5.234 ± 0.183	12368.3450	4.077 ± 0.057
11840.5390	5.027 ± 0.103	12369.2769	4.188 ± 0.022
11842.4730	5.388 ± 0.206	12381.2620	4.039 ± 0.125
11843.5660	5.184 ± 0.439	12385.3530	4.388 ± 0.033
11844.4960	4.679 ± 0.072	12386.2840	4.481 ± 0.038
11847.5150	4.600 ± 0.062	12387.2960	4.401 ± 0.034
11853.5681	4.767 ± 0.049	12388.3290	4.504 ± 0.050
11866.4100	5.478 ± 0.233	12399.3050	4.898 ± 0.169
11867.3210	5.155 ± 0.197	12403.3180	5.097 ± 0.190
11868.3710	5.349 ± 0.190	12404.2690	5.073 ± 0.029
11869.4960	5.184 ± 0.073	12405.3055	5.015 ± 0.030
11878.4490	5.012 ± 0.080	12406.3010	5.193 ± 0.227
11879.2630	5.222 ± 0.212	12407.2730	4.971 ± 0.034
11882.4800	4.656 ± 0.170	12408.2942	5.104 ± 0.025
11901.3160	5.436 ± 0.106	12409.3480	5.078 ± 0.216
11902.2690	5.688 ± 0.205	12410.2870	5.132 ± 0.028
11912.5120	5.116 ± 0.190	12411.2860	5.119 ± 0.029
11926.2770	4.424 ± 0.056	12417.2820	5.289 ± 0.052
11932.4920	4.795 ± 0.184	12419.3020	5.272 ± 0.049
11959.2270	4.689 ± 0.129	12421.2880	5.175 ± 0.058
11999.2700	4.517 ± 0.112	12440.2860	5.165 ± 0.050
12030.4220	5.191 ± 0.100	12441.3590	5.067 ± 0.078
12050.4650	4.689 ± 0.087	12442.2850	5.123 ± 0.044
12104.3160	4.394 ± 0.069	12459.2830	5.198 ± 0.064
12139.5420	4.138 ± 0.196	12476.2920	5.265 ± 0.063
12144.5390	4.620 ± 0.200	12484.3370	4.793 ± 0.064
12147.5200	4.060 ± 0.155	12498.4950	4.379 ± 0.024
12166.5140	4.629 ± 0.167	12530.5830	4.424 ± 0.031
12174.5390	4.327 ± 0.069	12536.5580	4.640 ± 0.025
12175.5310	4.153 ± 0.084	12539.5520	4.732 ± 0.040
12192.5510	4.046 ± 0.095	12541.5710	4.653 ± 0.041
12199.5620	4.094 ± 0.151	12557.5940	4.579 ± 0.027
12201.5449	3.888 ± 0.054	12566.4570	4.422 ± 0.036
12210.5970	4.129 ± 0.149	12569.5400	4.648 ± 0.043
12223.5055	4.090 ± 0.060	12593.6361	4.954 ± 0.035
12225.3400	4.340 ± 0.161	12595.3070	4.844 ± 0.035
12231.5060	4.060 ± 0.151	12596.5600	4.890 ± 0.043
12263.4680	4.094 ± 0.024	12597.5780	4.956 ± 0.044
12265.5230	4.182 ± 0.140	12605.5350	5.416 ± 0.051
12280.5470	3.783 ± 0.020	12608.5690	5.428 ± 0.034
12281.4510	3.725 ± 0.018	12609.5610	5.467 ± 0.030
12283.4430	3.801 ± 0.020	12610.4815	5.324 ± 0.028
12298.4070	3.623 ± 0.022	12612.5340	5.550 ± 0.030
12301.3840	3.625 ± 0.028	12613.4293	5.497 ± 0.030
12307.2820	3.427 ± 0.129	12614.5590	5.548 ± 0.033
12308.3500	3.628 ± 0.019	12618.3620	5.532 ± 0.026
12309.4384	3.599 ± 0.019	12619.5547	5.452 ± 0.026
12310.4000	3.307 ± 0.128	12620.4070	5.375 ± 0.035
12313.4260	3.307 ± 0.132	12621.4710	5.477 ± 0.034
12314.3730	3.823 ± 0.030	12625.4390	5.301 ± 0.036
12316.4110	3.906 ± 0.020	12634.2880	4.730 ± 0.164
12321.4275	4.018 ± 0.023	12635.4457	5.088 ± 0.155
12322.4080	4.144 ± 0.023	12636.3986	5.035 ± 0.042
12323.3560	4.108 ± 0.021	12665.3620	4.728 ± 0.026
12324.3990	4.152 ± 0.126	12672.3350	4.974 ± 0.038
12336.2490	3.507 ± 0.110	12674.4100	5.041 ± 0.031
12342.4700	3.402 ± 0.144	12675.3846	5.002 ± 0.028

**Table 3** – *continued* Combined F5170 continuum fluxes from spectral and photometric observations.

JD-2,440,000	F5170	Julian Date	F5170
12343.4263	3.559 ± 0.046	12683.3540	4.635 ± 0.037
12346.3890	3.499 ± 0.132	12684.3840	4.703 ± 0.034
12348.2790	3.315 ± 0.141	12685.3890	4.632 ± 0.051
12689.3540	4.830 ± 0.041	12998.4690	4.207 ± 0.024
12694.3330	4.772 ± 0.034	13003.4349	4.187 ± 0.022
12696.3900	5.087 ± 0.195	13006.4560	4.084 ± 0.056
12697.3620	4.836 ± 0.025	13007.4330	4.046 ± 0.034
12698.3500	4.913 ± 0.027	13015.4930	3.971 ± 0.057
12700.3786	4.836 ± 0.027	13022.4180	4.391 ± 0.024
12701.3560	4.781 ± 0.027	13023.3250	4.367 ± 0.143
12703.2680	4.711 ± 0.175	13058.3160	4.776 ± 0.026
12710.2760	4.595 ± 0.028	13071.4320	4.767 ± 0.072
12716.2540	4.167 ± 0.033	13073.3260	4.521 ± 0.033
12722.3690	4.069 ± 0.145	13077.3130	4.367 ± 0.136
12723.4030	3.889 ± 0.142	13083.3410	4.438 ± 0.030
12724.3289	4.009 ± 0.024	13084.3190	4.500 ± 0.029
12726.2940	3.771 ± 0.138	13084.3190	4.500 ± 0.029
12727.3100	4.033 ± 0.028	13085.3510	4.558 ± 0.028
12728.3020	4.123 ± 0.024	13087.2780	4.425 ± 0.028
12729.3010	4.177 ± 0.024	13089.3240	4.197 ± 0.062
12730.2840	4.232 ± 0.029	13097.2904	4.606 ± 0.041
12739.2820	4.235 ± 0.028	13098.2500	4.636 ± 0.038
12740.3020	4.185 ± 0.031	13105.3080	4.556 ± 0.152
12742.3080	4.205 ± 0.035	13111.3030	4.978 ± 0.027
12744.3070	4.221 ± 0.030	13112.3115	4.799 ± 0.025
12745.2760	4.272 ± 0.037	13113.3120	4.864 ± 0.028
12751.2799	4.242 ± 0.024	13114.2551	5.012 ± 0.030
12752.2510	4.309 ± 0.024	13115.2890	5.108 ± 0.029
12754.2770	4.383 ± 0.024	13117.3010	4.814 ± 0.164
12756.2860	4.324 ± 0.024	13130.2730	5.063 ± 0.044
12757.2770	4.296 ± 0.024	13133.2930	5.075 ± 0.026
12759.2830	4.647 ± 0.165	13135.2730	5.004 ± 0.029
12766.2680	4.454 ± 0.025	13148.2890	4.770 ± 0.030
12767.2590	4.544 ± 0.029	13149.2750	4.727 ± 0.045
12770.2590	4.320 ± 0.038	13153.2910	4.802 ± 0.032
12771.2560	4.272 ± 0.051	13154.3280	4.884 ± 0.052
12774.2750	4.356 ± 0.035	13277.5570	5.045 ± 0.079
12775.2710	4.353 ± 0.043	13291.5610	4.765 ± 0.029
12778.2980	4.492 ± 0.185	13292.5770	4.817 ± 0.029
12790.3080	4.933 ± 0.028	13296.6160	4.355 ± 0.027
12791.2820	4.859 ± 0.040	13300.6100	4.245 ± 0.029
12841.5450	4.824 ± 0.104	13302.6060	4.161 ± 0.029
12866.5290	5.115 ± 0.034	13305.6230	4.073 ± 0.027
12883.5410	5.011 ± 0.171	13307.6120	4.107 ± 0.053
12889.5360	5.408 ± 0.169	13308.6250	4.040 ± 0.046
12890.5250	5.376 ± 0.032	13309.6280	3.986 ± 0.039
12903.5440	5.300 ± 0.186	13313.6020	4.011 ± 0.027
12906.5980	5.109 ± 0.031	13314.5960	4.109 ± 0.027
12907.5800	4.926 ± 0.159	13315.6030	4.046 ± 0.024
12912.5813	5.089 ± 0.030	13317.5910	3.993 ± 0.027
12913.5490	5.132 ± 0.034	13318.6095	3.912 ± 0.028
12914.5768	5.108 ± 0.028	13319.4960	3.639 ± 0.065
12915.5268	5.260 ± 0.049	13320.4660	3.581 ± 0.116
12945.6380	4.830 ± 0.047	13323.5880	3.991 ± 0.133
12947.5950	4.664 ± 0.032	13331.5011	3.818 ± 0.021
12965.5343	4.463 ± 0.022	13355.4852	3.397 ± 0.019
12966.5492	4.309 ± 0.027	13356.4777	3.397 ± 0.022
12967.5156	4.435 ± 0.026	13357.4334	3.360 ± 0.018
12968.5385	4.372 ± 0.024	13358.4690	3.454 ± 0.021
12973.4510	4.025 ± 0.132	13365.5680	3.342 ± 0.037
12974.5110	3.982 ± 0.131	13379.5508	3.316 ± 0.019
12983.6310	4.241 ± 0.045	13383.4821	3.446 ± 0.019

**Table 3** – *continued* Combined F5170 continuum fluxes from spectral and photometric observations.

JD-2,440,000	F5170	Julian Date	F5170
12984.5580	4.277 ± 0.034	13384.4410	3.389 ± 0.020
12985.4810	4.329 ± 0.087	13410.4190	3.370 ± 0.113
12988.5170	4.372 ± 0.029	13411.5060	3.259 ± 0.106
12996.5188	4.248 ± 0.024	13412.3370	2.904 ± 0.097
12997.4890	4.193 ± 0.025	13419.3710	3.446 ± 0.047
13423.3570	3.454 ± 0.033	13822.3430	6.565 ± 0.043
13424.4630	3.439 ± 0.068	13823.3110	6.558 ± 0.044
13425.3360	3.493 ± 0.041	13830.2380	6.715 ± 0.113
13434.3090	3.703 ± 0.022	13837.3880	6.661 ± 0.051
13436.3070	3.791 ± 0.024	13839.3400	6.759 ± 0.068
13437.2730	3.483 ± 0.114	13844.3300	6.879 ± 0.040
13441.3348	3.908 ± 0.021	13845.4410	6.959 ± 0.047
13445.2997	4.160 ± 0.024	13849.2870	7.053 ± 0.251
13446.3470	4.388 ± 0.042	13850.2917	7.117 ± 0.041
13449.3550	4.369 ± 0.034	13854.2850	7.053 ± 0.220
13459.3238	4.875 ± 0.026	13875.3320	7.178 ± 0.086
13460.2620	4.978 ± 0.028	13880.3050	6.746 ± 0.036
13461.2693	5.067 ± 0.027	13881.2850	6.795 ± 0.041
13462.3190	5.040 ± 0.032	13953.5550	6.732 ± 0.106
13464.2240	5.285 ± 0.037	13959.5530	6.737 ± 0.080
13465.3125	5.363 ± 0.031	13967.5620	6.846 ± 0.056
13471.2810	5.882 ± 0.206	13973.5680	6.731 ± 0.050
13476.3240	5.693 ± 0.037	13986.5780	7.163 ± 0.090
13478.2290	5.844 ± 0.111	13987.4830	7.138 ± 0.066
13487.2960	5.574 ± 0.029	13989.5540	7.280 ± 0.091
13493.2990	5.485 ± 0.029	13991.5330	7.168 ± 0.069
13495.2680	5.497 ± 0.034	13994.5660	7.272 ± 0.080
13508.3130	5.755 ± 0.037	13995.5930	7.363 ± 0.054
13509.2980	5.987 ± 0.045	14010.5960	7.574 ± 0.066
13611.5630	6.791 ± 0.081	14013.6130	7.494 ± 0.089
13612.5531	6.801 ± 0.083	14022.5790	7.319 ± 0.058
13621.5230	6.877 ± 0.082	14023.4520	7.557 ± 0.061
13641.5660	6.279 ± 0.096	14038.5550	7.741 ± 0.089
13644.5290	5.884 ± 0.039	14044.6030	8.011 ± 0.123
13645.6130	5.900 ± 0.076	14048.5820	7.691 ± 0.097
13647.5700	6.158 ± 0.095	14059.5450	7.104 ± 0.047
13648.6094	5.937 ± 0.048	14060.6550	6.988 ± 0.147
13649.5913	6.174 ± 0.075	14062.5450	7.171 ± 0.054
13650.6170	5.939 ± 0.054	14064.5904	7.159 ± 0.049
13651.5770	5.914 ± 0.040	14065.4730	7.052 ± 0.036
13653.6120	5.885 ± 0.031	14067.5428	6.865 ± 0.045
13654.5950	5.972 ± 0.038	14069.6400	6.920 ± 0.056
13670.5550	6.284 ± 0.083	14076.4610	6.903 ± 0.156
13676.5860	6.309 ± 0.079	14078.5510	6.923 ± 0.101
13680.5980	5.868 ± 0.033	14086.5590	7.182 ± 0.097
13683.5360	5.688 ± 0.189	14091.5530	7.180 ± 0.044
13698.4690	6.366 ± 0.103	14106.5310	7.897 ± 0.243
13702.4780	5.872 ± 0.203	14111.5780	7.450 ± 0.050
13708.5590	6.684 ± 0.036	14116.4500	7.638 ± 0.059
13724.5730	7.009 ± 0.049	14117.5520	7.552 ± 0.331
13728.3990	6.749 ± 0.217	14118.4140	7.587 ± 0.055
13733.5160	6.918 ± 0.039	14119.4440	7.704 ± 0.051
13738.4460	6.940 ± 0.046	14121.5630	7.700 ± 0.047
13739.5320	6.813 ± 0.047	14123.4870	7.720 ± 0.064
13744.5540	6.880 ± 0.047	14142.5940	7.459 ± 0.097
13747.4950	6.735 ± 0.078	14145.3596	7.674 ± 0.049
13749.4240	6.698 ± 0.070	14146.4190	7.550 ± 0.044
13760.3710	6.082 ± 0.030	14149.4380	7.735 ± 0.041
13761.4160	6.143 ± 0.042	14150.4260	7.695 ± 0.038
13763.3990	5.901 ± 0.035	14156.2700	7.366 ± 0.132
13774.4530	5.677 ± 0.189	14167.3450	7.289 ± 0.050
13787.3870	6.090 ± 0.203	14169.2930	7.252 ± 0.048



**Table 3** – *continued* Combined F5170 continuum fluxes from spectral and photometric observations.

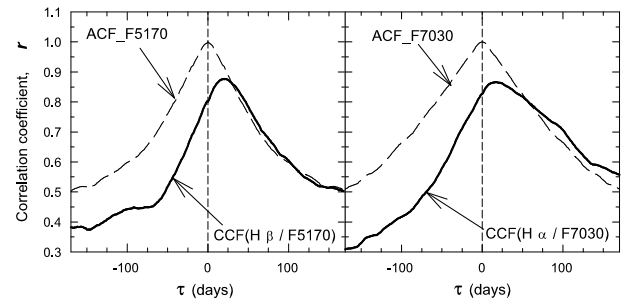
JD-2,440,000	F5170	Julian Date	F5170
13788.3440	5.997 ± 0.091	14171.3070	7.250 ± 0.050
13790.2820	6.259 ± 0.199	14174.4000	7.481 ± 0.243
13799.2870	6.168 ± 0.046	14180.3510	7.516 ± 0.260
13807.3650	6.250 ± 0.057	14181.2360	7.412 ± 0.042
13816.4150	6.349 ± 0.041	14191.2710	7.835 ± 0.083
13820.3430	6.248 ± 0.208	14200.3340	8.249 ± 0.058
14201.2850	7.755 ± 0.269	14523.3480	6.185 ± 0.197
14204.2350	8.256 ± 0.058	14530.3709	6.735 ± 0.064
14206.3000	8.379 ± 0.073	14532.3500	6.735 ± 0.044
14213.2460	7.978 ± 0.049	14534.3240	6.662 ± 0.036
14220.2400	8.159 ± 0.108	14535.3485	6.570 ± 0.031
14234.2640	8.173 ± 0.060	14536.3470	6.542 ± 0.038
14281.2840	8.751 ± 0.203	14537.3175	6.452 ± 0.051
14283.2890	8.724 ± 0.117	14538.3130	6.436 ± 0.062
14331.5430	8.416 ± 0.086	14542.2750	6.073 ± 0.056
14337.5760	8.331 ± 0.118	14554.3231	6.021 ± 0.030
14338.5040	8.265 ± 0.051	14555.2970	5.994 ± 0.093
14369.5160	7.978 ± 0.124	14565.4980	5.939 ± 0.037
14370.5390	7.390 ± 0.197	14567.2910	5.906 ± 0.034
14371.4990	7.464 ± 0.073	14568.2830	6.029 ± 0.043
14372.4860	7.718 ± 0.071	14574.2652	6.262 ± 0.052
14376.5510	7.373 ± 0.061	14582.4170	6.398 ± 0.035
14377.5820	7.570 ± 0.110	14585.2780	6.093 ± 0.046
14386.4570	7.490 ± 0.098	14586.3090	6.284 ± 0.086
14391.6032	7.187 ± 0.051	14587.2927	6.252 ± 0.034
14392.5390	7.115 ± 0.097	14588.2802	6.184 ± 0.054
14393.5960	7.037 ± 0.045	14590.3090	6.278 ± 0.098
14423.5722	6.184 ± 0.037	14591.2730	6.440 ± 0.108
14425.6040	6.198 ± 0.032	14596.3030	6.331 ± 0.101
14426.5370	6.223 ± 0.047	14600.2710	6.832 ± 0.055
14428.4230	6.298 ± 0.058	14601.3560	6.695 ± 0.093
14434.4860	6.146 ± 0.044	14602.3840	6.727 ± 0.057
14438.4380	5.934 ± 0.100	14603.3040	6.667 ± 0.051
14439.6060	6.055 ± 0.034	14604.3070	6.752 ± 0.056
14443.5395	6.118 ± 0.031	14617.2919	6.978 ± 0.059
14444.5270	6.180 ± 0.033	14618.2730	6.876 ± 0.087
14465.4540	7.011 ± 0.042	14620.3010	7.053 ± 0.091
14467.5530	7.210 ± 0.043	14622.4260	7.140 ± 0.087
14472.4660	7.411 ± 0.041	14628.3120	6.876 ± 0.046
14475.4050	6.727 ± 0.227	14632.3170	6.960 ± 0.075
14476.4683	7.358 ± 0.048	14643.3460	7.117 ± 0.044
14477.4660	7.463 ± 0.058	14647.3060	7.129 ± 0.041
14478.4300	7.452 ± 0.053	14687.5470	6.498 ± 0.095
14479.4230	7.456 ± 0.053	14713.5470	7.087 ± 0.267
14480.4251	7.368 ± 0.049	14718.5400	7.288 ± 0.051
14481.4803	7.412 ± 0.054	14720.5630	7.213 ± 0.227
14482.4074	7.451 ± 0.053	14738.5060	7.030 ± 0.237
14483.4110	7.452 ± 0.069	14740.4520	7.053 ± 0.241
14484.3690	7.183 ± 0.069	14742.5900	7.451 ± 0.051
14488.4530	7.111 ± 0.120	14769.5830	8.158 ± 0.265
14490.4630	7.314 ± 0.062	14778.5960	8.054 ± 0.050
14496.4231	7.715 ± 0.044	14779.6064	8.005 ± 0.041
14497.4230	7.654 ± 0.054	14780.5790	8.052 ± 0.042
14498.4680	7.550 ± 0.051	14781.5400	7.969 ± 0.048
14499.4361	7.641 ± 0.045	14784.3780	8.013 ± 0.128
14500.4060	7.739 ± 0.050	14786.4900	8.206 ± 0.084
14502.4057	7.653 ± 0.052	14796.4990	8.174 ± 0.050
14503.4437	7.605 ± 0.045	14799.6310	8.263 ± 0.061
14508.4223	7.310 ± 0.034	14801.3500	8.467 ± 0.064
14512.5400	6.981 ± 0.131	14802.5980	8.346 ± 0.052
14522.2720	6.496 ± 0.211	14804.5660	8.214 ± 0.093

 Continuum fluxes are in units  $10^{-15} \text{ ergs cm}^{-2} \text{ s}^{-1} \text{ \AA}^{-1}$ 
**Table 4.** Light curve statistics.

Time series <sup>a</sup>	N	dt-med (days)	Mean Flux <sup>b</sup>	std <sup>b</sup>	$F_{var}$	$R_{max}$
(1)	(2)	(3)	(4)	(5)	(6)	(7)
1992–2008, JD2448630–2454804						
F5170s	235	14	6.093	1.101	0.18±0.03	2.65±0.06
F5170scp	742	3	5.780	1.277	0.22±0.05	3.16±0.08
H $\beta$	235	14	4.065	0.658	0.16±0.03	2.70±0.09
F7030s	102	29	6.897	1.261	0.18±0.04	2.43±0.17
H $\alpha$	102	29	32.06	3.77	0.11±0.02	1.83±0.09

<sup>a</sup> The letters in the first column indicate the origin of the continuum fluxes: "s" – from the spectral observations only and "scp" – from combined spectral and photometric observations ("c" – CCD photometry, "p" – photoelectric photometry).

<sup>b</sup> Mean fluxes and standard deviations (std) are in units of  $10^{-13} \text{ erg cm}^{-2} \text{ s}^{-1}$  and  $10^{-15} \text{ erg cm}^{-2} \text{ s}^{-1} \text{ \AA}^{-1}$  for the lines and the continuum, respectively.


**Figure 4.** CCFs of Mrk 6 between the H $\beta$  and continuum F5170 fluxes (left panel) as well as between the H $\alpha$  and continuum F7090 in 1993–2008 (thick lines). ACFs are shown by dashed lines.

lines (the correlation coefficients are equal to 0.93 and 0.97, respectively). The positive lag values for the 'H $\alpha$ –H $\beta$ ' and 'F7030–F5170' light curves mean that the region of effective continuum emission at  $\lambda 5170$  is probably smaller than that at  $\lambda 7030$  and the region of effective H $\beta$  emission is probably smaller than that H $\alpha$ . The probability that the delay for the 'F7030–F5170' and 'H $\alpha$ –H $\beta$ ' is less than zero equals to 0.023 and 0.036, respectively.

**Table 5.** Cross-correlation results for 1993–2008.

First set	Second set	$r_{max}$	$\tau_{cn}$	$\tau_{pk}$
H $\beta$	F5170s	0.84	21.5 <sup>+3.9</sup> <sub>-2.1</sub>	21.0 <sup>+1.6</sup> <sub>-4.9</sub>
H $\beta$	F5170scp	0.83	21.9 <sup>+2.6</sup> <sub>-2.7</sub>	21.0 <sup>+1.2</sup> <sub>-4.0</sub>
H $\alpha$	F7030s	0.88	31.6 <sup>+10.9</sup> <sub>-8.4</sub>	18.0 <sup>+8.3</sup> <sub>-6.4</sub>
H $\alpha$	F5170scp	0.85	26.8 <sup>+10.6</sup> <sub>-4.8</sub>	22.0 <sup>+6.9</sup> <sub>-6.9</sub>
H $\alpha$	H $\beta$	0.93	8.5 <sup>+8.6</sup> <sub>-4.2</sub>	2.5 <sup>+0.4</sup> <sub>-1.6</sub>
F7030s	F5170s	0.97	7.2 <sup>+3.7</sup> <sub>-4.4</sub>	5.5 <sup>+2.5</sup> <sub>-1.5</sub>
F7030s	F5170scp	0.96	8.4 <sup>+2.1</sup> <sub>-3.6</sub>	3.2 <sup>+4.4</sup> <sub>-1.8</sub>
H $\gamma$	F5170sc	0.53	33.1 <sup>+9.2</sup> <sub>-11.6</sub>	27.1 <sup>+17.1</sup> <sub>-5.9</sub>
H $\gamma$	H $\beta$	0.82	8.9 <sup>+8.1</sup> <sub>-9.1</sub>	-0.6 <sup>+18.3</sup> <sub>-2.3</sub>

Meaning of symbols "s" and "scp" the same as in Table4.

**Table 6.** Time intervals for time series analysis in the H $\beta$  region.

Time Series	JD2440000+	N		$\Delta t_{med}$	
		H $\beta$	cont <sup>a</sup>	H $\beta$	cont
1	09250–09872	38	51 sp	14.0	8.9
2	09980–10777	54	90 sp	11.9	3.0
3	10869–11516	27	59 sp	16.0	6.1
4	11557–13356	47	266 scp	19.1	2.0
5	13611–14804	58	242 scp	10.8	2.1

<sup>a</sup> Meaning of symbols "sp" and "scp" is the same as in Table 4.

The time interval 1993–2008, that has been used for cross-correlation analysis, is very long. We have divided it into five subinterval in order to check whether the lag values for individual sub-intervals are the same as for the entire 1993–2008 period, whether they are changed in time, and whether they are correlated with the fluxes and with line widths. In particular, the effective region of the broad-line emission can depend on the incident continuum flux, so the lag can depend on the continuum flux. Under a virialized motion of the line-emitting gas the expected relation between the lag  $\tau$  and the line width  $V$  is as follows:  $V \propto \tau^{-1/2}$ . To this end, we used only the H $\beta$  spectra because more reliable lag estimate for this line, and we carried out the cross-correlation analysis separately for each of the five time intervals listed in the Table 6. The first and second intervals were taken the same as in the paper by Sergeev et al. (1999).

The cross-correlation results for the five time subintervals are given in Table 7. For the continuum light curve in Table 7 that consists of the spectral data only (i.e., when the number of data points in both the H $\beta$  and continuum light curves is the same) we have used the standard method of the CCF computation with the rebinning both time series. When the photometric data are added to the continuum light curve, only the continuum light curve was rebinned to the times of observation of the H $\beta$  light curve. As for the entire period, the lag uncertainties for the individual subintervals were computed by using the FR/RSS method as given by Peterson et al. (1998). The uncertainties for each subinterval were computed using 4000 FR/RSS realizations, and the probability distributions for both  $\tau_{cn}$  and  $\tau_{pk}$  were calculated. Each of these distributions was found to be very different from the normal distribution. **To obtain the unweighted mean lag and its uncertainties we have sequentially (one after another) performed the convolution of the five individual distributions and then we have scaled the  $\tau$ -axis by dividing it by a number of subintervals (i.e., by five). After the convolution operation, the final probability distribution was found to be almost normal with the expectation and standard deviation as given in Table 7 for the mean lag.**

Since there are large gaps in our time series, we decided to investigate in more detail their effect on the lag uncertainties for Mrk 6. To make sure that the uncertainties in our lag estimates are realistic, we decided to verify the effect of the sampling of our time series to the lag determination and to compare results with those obtained by random subset selection (RSS) method. We have generated random time series with the same autocorrelation function

**Table 7.** Cross-correlation results for the H $\beta$  line for the five subintervals.

Subset Number	N points		$\tau_{cn}$	$\tau_{pk}$	$\tau_{max}$
	H $\beta$	F5170			
1	38	38	22.7 <sup>+7.4</sup> <sub>-3.0</sub>	20.5 <sup>+4.7</sup> <sub>-2.8</sub>	0.939
2	54	54	20.8 <sup>+3.0</sup> <sub>-2.6</sub>	18.1 <sup>+3.6</sup> <sub>-1.0</sub>	0.942
3	27	27	19.3 <sup>+4.0</sup> <sub>-6.0</sub>	18.2 <sup>+7.7</sup> <sub>-6.1</sub>	0.761
4	47	199 <sup>a</sup>	26.2 <sup>+12.3</sup> <sub>-6.8</sub>	14.2 <sup>+14.6</sup> <sub>-1.4</sub>	0.898
5	58	230 <sup>a</sup>	20.2 <sup>+5.0</sup> <sub>-3.9</sub>	26.8 <sup>+0.3</sup> <sub>-13.8</sub>	0.794
Mean value:			21.4 $\pm$ 2.0	19.3 $\pm$ 1.9	
1	38	51 <sup>b</sup>	21.2 <sup>+4.0</sup> <sub>-3.2</sub>	21.0 <sup>+4.0</sup> <sub>-3.4</sub>	0.923
2	54	90 <sup>b</sup>	20.7 <sup>+3.0</sup> <sub>-2.4</sub>	22.0 <sup>+1.3</sup> <sub>-4.7</sub>	0.939
3	27	59 <sup>b</sup>	20.5 <sup>+5.6</sup> <sub>-7.0</sub>	28.5 <sup>+1.4</sup> <sub>-21.9</sub>	0.683
4	47	266 <sup>c</sup>	23.9 <sup>+17.0</sup> <sub>-7.3</sub>	9.5 <sup>+15.6</sup> <sub>-1.2</sub>	0.881
5	58	242 <sup>c</sup>	20.4 <sup>+4.6</sup> <sub>-4.1</sub>	21.8 <sup>+5.1</sup> <sub>-8.7</sub>	0.803
Mean value			21.1 $\pm$ 1.9	20.5 $\pm$ 2.2	

<sup>a</sup> Continuum light curve was combined from the spectral data and from the CCD photometry.

<sup>b</sup> Continuum light curve was combined from the spectral data and from the photoelectric photometry.

<sup>c</sup> Continuum light curve was combined from the spectral data and from both the CCD and photoelectric photometry.

as observed ACF. Stationary random process (or time series) with a given ACF can be generated from an array of *independent* random values  $\xi_1, \xi_2, \xi_3, \dots, \xi_n$ . To do this, it is necessary to find a matrix  $U_{ij}$ , such that the multiplication of the matrix  $U$  to the vector  $\xi$  gives a vector of *dependent* random values  $x_1, x_2, x_3, \dots, x_n$ , with a given correlation matrix  $\rho_{ij} = ACF(t_j - t_i)$ , where  $t_1, t_2, t_3, \dots, t_n$  are times of observations. The matrix  $U$  is related to the correlation matrix  $\rho$  as follows:

$$\rho = U U^T, \quad (1)$$

where  $T$  denotes a transposition operation. We used our own algorithm to compute the matrix  $U$  from ACF.

First we have generated 1000 realizations of the continuum light curve with a time resolution of 1 day over a period of 6452 days, which is longer than the real observed time interval (6175 days).

To simulate the H $\beta$  light curve from the continuum light curve we have experimented with the three kinds of transfer functions: (1) delta-function  $\delta(\tau - 20)$ , (2) II-shaped function which is a constant for  $0 < \tau < 40$ , and (3) triangular function which is linearly decreased down to a zero value from  $\tau = 0$  to  $\tau = 68.3$ . Here the lag  $\tau$  are in units of days. After the convolution with the simulated continuum light curves, all the transfer functions give the H $\beta$  light curve with a lag of about 20 days. Next the simulated continuum and line light curves were rebinned to real moments of observations and the cross-correlation functions were computed for each realization. The lag peak and centroid were measured. The largest uncertainties were obtained when we used the triangular transfer function. These uncertainties are only due

to the sampling of the observation data. Table 8 gives a comparison of both methods for uncertainty estimates (i.e., the random time series versus RSS method) for the triangular transfer function. The columns designated as  $\tau_{pk}$  and  $\tau_{cn}$  are a lag with  $\pm 1\sigma$  uncertainties computed from the random time series, while other two columns designated as RSS give  $\pm 1\sigma$  uncertainties computed from RSS method for  $\tau_{pk}$  and  $\tau_{cn}$ , respectively. The last column of the table is the mean CCF peak value obtained from the method of the random time series. As can be seen from this table, the RSS method gives comparable or larger (up to two times) uncertainties than the method of the random time series does. The random time series method seems to be more direct way to estimate lag uncertainties and since the lag uncertainties were computed in this paper by the RSS method, they seem to be realistic or slightly overestimated.

There is a contradiction between our lag estimate and the preliminary results on Mrk 6 published in a conference proceeding by Grier et al. (NASA ADS tag 2011nlsq.confE..52G). This new campaign had a nightly sampling rate and it spanned 125 nights beginning 2010 August 31 and ending on 2011 January 3. They claimed a lag of  $8 \pm 3$  days for the H $\beta$  line in Mrk 6. We have first checked the effect of the removing of linear trends from our light curves (**as recommended by some authors, e.g., Welsh 1999**). We have removed linear trends from the H $\beta$  and continuum light curves for each subinterval, even if there are no such trends exist. Then we have recalculated a mean lag value and it was to be 19 days, i.e. two days less. Then we have generated random time series (continuum and H $\beta$ ) by exactly the same way as described above, but for the sampling rate of Grier et al. in order to check whether the duration of the monitoring program is important for the lag measurements. We found that with the data sampling of Grier et al. our lag estimate must be less by one more day, and so a total difference between our and their results must be three days. The real difference is much larger than three days. An unexpected result of our simulation was very large lag uncertainties for the 125-days data sampling and for the triangular transfer function for the H $\beta$  line (see above). The lag uncertainties were found to be as large as  $\pm 6$  days! However, for the  $\delta(\tau - 20)$  transfer function (i.e., when the line light curve is simply a shifted version of the continuum light curve) the lag uncertainties were found to be as small as  $\sim 0.1$  days. So, for short-term campaigns and for transfer functions with a long tail (i.e., when the line light curve is not only shifted, but a strongly smoothed version of the continuum light curve), the uncertainties in lag estimates can be very large and they are connected to the extrapolation of the line and continuum fluxes when computing the CCF, not to the data sampling. We concluded that we can only explain the difference of three days between our and their lag measurements. Probably, the rest of the difference is due to real changes of lag or due to the measurement uncertainties and their underestimation.

It can be seen from Table 8 that the simulated lag values are almost the same for all subinterval. The expected lag value can be obtained by convolving the ACF with the transfer function and it was found to be:  $\tau_{pk} = 20.7$  days and  $\tau_{cn} = 22.4$  day in an excellent agreement with the simulation results. So, the large gaps in our time series do not shift the lag measurements.

**Table 8.** Comparison of the lag uncertainty estimates between the method of the random time series and the RSS method.

Interval	$\tau_{pk}$	RSS	$\tau_{cn}$	RSS	$r_{sim}$
1	$20.8^{+2.4}_{-2.1}$	2.1	$22.2^{+2.8}_{-2.8}$	2.7	0.968
2	$20.8^{+1.5}_{-1.6}$	1.6	$22.2^{+2.8}_{-2.8}$	2.1	0.960
3	$20.5^{+2.8}_{-2.8}$	6.0	$22.4^{+4.6}_{-4.6}$	4.3	0.940
4	$20.4^{+2.6}_{-2.6}$	3.4	$22.1^{+4.4}_{-4.0}$	8.5	0.980
5	$20.6^{+2.4}_{-2.7}$	6.9	$22.4^{+3.7}_{-3.5}$	3.3	0.978

**Table 9.** The broad H $\beta$ , and H $\alpha$  line width measurements for 1993–2008.

	FWHM	$\sigma_{line}$
	km s $^{-1}$	
H $\beta$ (mean-spectrum)	$6278 \pm 378$	$2821 \pm 13$
H $\beta$ (RMS-spectrum)	$5445 \pm 468$	$2884 \pm 97$
H $\alpha$ (mean-spectrum)	$5322 \pm 142$	$2870 \pm 22$
H $\alpha$ (rms-spectrum)	$4443 \pm 338$	$2780 \pm 35$

#### 4 LINE WIDTH MEASUREMENTS

It is well known that the emission-line profile evolution cannot be entirely attributed to the reverberation effect and that the profile changes usually occur on a time scale that is much longer than the flux-variability time scale (see Wanders & Peterson 1996). To decrease the effect of the long-term profile changes on the line width measurements and to get sufficient statistics, we measured the H $\beta$  and H $\alpha$  line widths for the five subintervals presented in Table 6. The line width is typically characterized by its full width at half maximum (FWHM) or by the second moment of the line profile, denoted as  $\sigma_{line}$ . To measure FWHM for the mean H $\alpha$  and H $\beta$  line profiles, we removed narrow lines from the broad line profiles. This is not required for rms profiles. However, the spectra must be optimally aligned in wavelength and in spectral resolution in order to reduce the narrow line residuals in the rms profiles. It is difficult to measure FWHM because both the mean broad and rms H $\beta$  profiles are double-peaked, and so the scatter in the FWHM measurements is much larger than in  $\sigma_{line}$  which is well defined for arbitrary line profiles. The uncertainties in the line width were obtained using bootstrap method described by Peterson et al. (2004). The H $\beta$  and H $\alpha$  line width (both FWHM and  $\sigma_{line}$ ) and their uncertainties are listed in Table 9 for 1993–2008. Table 10 gives the  $\sigma_{line}$  computed separately for each considered subinterval and for the H $\beta$  line only.

We examined the relationship between the H $\beta$  lag, H $\beta$  width, and the continuum flux (see Fig. 5). No significant correlations among above three parameters were found. In particular, the virial relationship between the lag and width does not contradict to our data, but the correlation coefficient between them does not differ significantly from the zero value. More subintervals and less lag uncertainties are required.

**Table 10.** Results for the five subintervals

Time series	Mean Flux <sup>a</sup>		$\tau_{cn}$ days	$\sigma_{line}$ km s <sup>-1</sup>		$M_{BH}^b$ in units $10^8 M_\odot$	
	F(5170)	F(H $\beta$ )		(mean)	(rms)	(mean)	(rms)
1	2	3	4	5	6	7	8
1	6.446	3.632	21.2 <sup>+4.0</sup> <sub>-3.2</sub>	2813 $\pm$ 13	2836 $\pm$ 48	1.77 <sup>+0.33</sup> <sub>-0.27</sub>	1.80 <sup>+0.34</sup> <sub>-0.28</sub>
2	6.472	3.976	20.7 <sup>+3.0</sup> <sub>-2.4</sub>	2804 $\pm$ 6	2626 $\pm$ 37	1.72 <sup>+0.25</sup> <sub>-0.20</sub>	1.50 <sup>+0.22</sup> <sub>-0.18</sub>
3	5.730	3.587	20.5 <sup>+5.6</sup> <sub>-7.0</sub>	2808 $\pm$ 14	2876 $\pm$ 46	1.70 <sup>+0.46</sup> <sub>-0.58</sub>	1.79 <sup>+0.49</sup> <sub>-0.61</sub>
4	4.594	2.677	23.9 <sup>+17.0</sup> <sub>-7.3</sub>	2870 $\pm$ 13	3222 $\pm$ 39	2.07 <sup>+1.50</sup> <sub>-0.63</sub>	2.62 <sup>+1.80</sup> <sub>-0.80</sub>
5	7.027	3.523	20.4 <sup>+4.6</sup> <sub>-4.1</sub>	2807 $\pm$ 8	2864 $\pm$ 35	1.69 <sup>+0.38</sup> <sub>-0.34</sub>	1.77 <sup>+0.40</sup> <sub>-0.36</sub>
Average:			21.1 $\pm$ 1.9	2812 $\pm$ 10 <sup>c</sup>	2882 $\pm$ 100 <sup>c</sup>	1.76 $\pm$ 0.16	1.85 $\pm$ 0.21

<sup>a</sup> Same flux units as in Table 1 for 5170 Å continuum and H $\beta$ , respectively.

<sup>b</sup> Using Onken et al (2004) calibration,  $f = 5.5$ .

<sup>c</sup> **The line width and uncertainties were computed as weighted average and assuming different expectations of the line widths among individual periods of observations.**

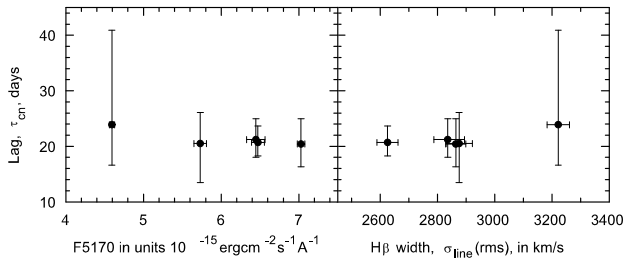


**Figure 5.** The relation between the continuum flux and the lag ( $\tau_{cn}$ ) for H $\beta$  in Mrk 6, as well as between the H $\beta$  width and the lag ( $\tau_{cn}$ ).

## 5 BLACK HOLE MASS OF MRK 6

Determination of the black hole mass from reverberation mapping rests upon the assumption that the gravity of the central super-massive black hole dominates over gas motions in the BLR. The black hole mass is defined by the virial equation

$$M_{BH} = f \frac{c\tau(\Delta V)^2}{G},$$

where  $\tau$  is the measured emission-line time delay,  $c$  is the speed of light,  $c\tau$  represents the BLR size, and  $\Delta V$  is the BLR velocity dispersion. The dimensionless parameter  $f$  is the scaling factor, which depends on the BLR structure, kinematics and inclination of BLR. Peterson et al. (2004) argued that  $\tau_{cn}$  for the time delay  $\tau$ , and  $\sigma_{line}$ , measured from the H $\beta$  emission line in the rms spectrum for the emission line width  $\Delta V$ , provide the most robust estimates of the black hole mass with the reverberation technique. Later Collin et al. (2006) confirmed that in most cases for the black hole mass estimate the line dispersion  $\sigma_{line}$  is more suitable than the FWHM, and  $\sigma_{line}$  from the rms-spectrum is more suitable than the  $\sigma_{line}$  from the mean spectrum.

We adopt an average value of  $f = 5.5$  based on the assumption that AGNs follow the same  $M_{BH} - \sigma_*$  relationship as quiescent galaxies (Onken et al. 2004). This is consistent with Woo et al. (2010) and allows easy comparison with pre-

vious results, but this is about a factor of two larger than the value of  $f$  computed by Graham et al. (2011). The value of  $f$  can be more decreased due to the effect of radiation pressure, as was explored by Marconi et al. (2008, 2009). Marconi et al. suggested that neglecting the effect of radiation pressure can lead to underestimation of the true black hole mass, especially in objects close to their Eddington limit. Discussion between Marconi et al. (2008, 2009) and Netzer (2009) shows that there are many unclear questions in this area. Naturally, a corrective term for radiation pressure will decrease the  $f$ -factor.

We calculated the black hole mass for Mrk 6 with the use of  $\tau_{cn} = 21.1 \pm 1.9$  for the time delay averaged over five time intervals and  $\sigma_{line} = 2882 \pm 100$  km s<sup>-1</sup> from the rms spectra for H $\beta$ . With  $\tau_{cn}$  taken in days and ( $\Delta V$ ) in km s<sup>-1</sup>, and taking into account the time dilation correction for the value of  $\tau_{cn}$ , the mass is equal to:

$$M_{BH}/M_\odot = 0.1952 \times f \times \frac{\tau_{cn}(obs)}{(1+z)} \times (\Delta V)^2.$$

The black hole mass calculated from the H $\beta$  line is  $(1.85 \pm 0.21) \times 10^8 M_\odot$ . For the H $\alpha$  line, the  $\tau_{cn} = 26.8 \pm 7.7$  days and  $\sigma_{line} = 2780 \pm 35$  km s<sup>-1</sup> and the black hole mass is equal to  $(2.2 \pm 0.6) \times 10^8 M_\odot$ .

The black hole masses calculated for each of five periods of observations are listed in columns 7 and 8 of Table 10 for the  $\sigma_{line}$  from the mean and rms spectra. One can see that all the estimates of the black hole mass based on the H $\beta$  line are the same within the scatter.

## 6 THE BLR SIZE–LUMINOSITY AND MASS–LUMINOSITY RELATIONSHIPS

Many characteristics of the Mrk 6 galaxy are typical for active galaxies. In this connection, it is of interest to see the localization of this galaxy on the BLR Radius–Luminosity and Mass–Luminosity diagrams. These diagrams determine a relationship between fundamental characteristics of AGNs. To this end, the Mrk 6 luminosity should be known. Up to the present, for many AGNs the luminosity in the rest-frame  $\lambda_0 = 5100$  Å has been corrected for host-galaxy starlight

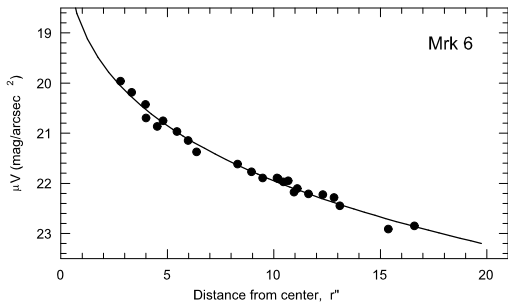


**Figure 6.** Surface brightness distribution for Mrk 6 in the V-band on the basis of multi-aperture photoelectric photometry by Neizvestny (1987). The solid curve corresponds to the model  $\mu(r) = a + br + cr^{1/4}$ .

contribution within the apertures used in spectral observations (see Bentz et al. 2009a). These authors used high-resolution *Hubble Space Telescope* (HST) images to measure the starlight contribution. This contribution was found to be significant, especially for low-luminosity AGNs.

We tried to get at least a rough estimate of the host-galaxy contribution using the observations made by Neizvestny (1987) at the Special Astrophysical Observatory (SAO) in October 1984 with different apertures from  $A=4''.3$  to  $55''$ . The surface brightness distribution in the host galaxy of the Mrk 6 nucleus calculated on the basis of these measurements is shown in Fig. 6.

The galaxy contribution in our  $3'' \times 11''$  spectral window was found to be  $V_{gal}=15^m6$  or  $F_{gal}=2.08 \times 10^{-15} \text{ erg s}^{-1} \text{ cm}^{-2} \text{ \AA}^{-1}$ . The mean flux observed in the continuum near  $\lambda_0=5100 \text{ \AA}$  is  $F_{(gal+nuc)}=6.093 \times 10^{-15} \text{ erg s}^{-1} \text{ cm}^{-2} \text{ \AA}^{-1}$  (see Table 4) and, thus, the mean flux corrected for the galaxy contribution is equal to  $F_{nuc}=4.013 \times 10^{-15} \text{ erg s}^{-1} \text{ cm}^{-2} \text{ \AA}^{-1}$ . The variability amplitude  $F_{var}$  increases from 18% to 27% after accounting for the galaxy contribution. The mean flux was also corrected for Galactic reddening according to the NASA/IPAC Extragalactic Database (NED) Schlegel et al. (1998). The luminosity was found to be  $\lambda L_{\lambda}(5100)=(2.51 \pm 0.78) \times 10^{43} \text{ erg s}^{-1}$  adopting the galaxy distance  $D=81 \text{ Mpc}$  and when the galaxy contribution is removed.

The bolometric luminosity of the Mrk 6 nucleus was adopted to be  $L_{bol} \simeq 9\lambda L_{\lambda}(5100\text{\AA})$  according to Kaspi et al. (2000) and it is equal to  $L_{bol}(nucl)=2.26 \times 10^{44} \text{ erg s}^{-1}$ . This luminosity is far from the Eddington limit ( $L_{Edd}$ ), which is equal to  $L_{Edd}=2.16 \times 10^{46} \text{ erg s}^{-1}$  for a black hole mass of  $1.8 \times 10^8 M_{\odot}$ . In other words, the Eddington ratio for Mrk 6 is  $L_{bol}/L_{Edd} \simeq 0.01$ . In this case and because there are no clear indications of gas outflow from the BLR, the radiation pressure has a negligible effect on the reverberation mass estimate.

The position of the Mrk 6 nucleus on the BLR Size–Luminosity diagram is shown in Fig. 7. The BLR size and the luminosity of other galaxies in Fig. 7 are taken from Bentz et al. (2009a) and Denney et al. (2010). The black hole masses in Fig. 7 are taken from Peterson et al. (2004), except for the galaxies Mrk 290, Mrk 817, NGC 3227,

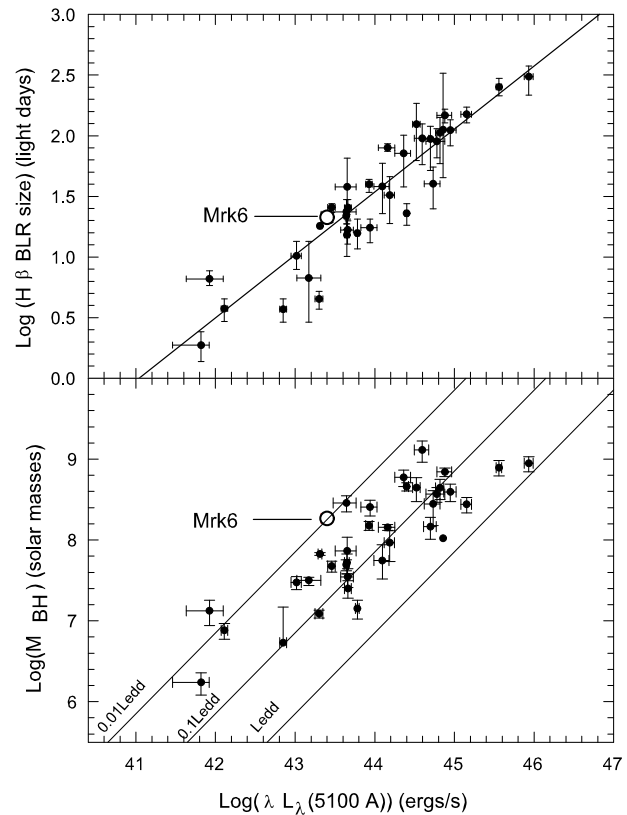


**Figure 7.** Top:  $H\beta$  BLR size vs. luminosity at  $5100\text{\AA}$  according to Bentz et al. (2009a) and Denney et al. (2010). The luminosity of all nuclei was corrected for host galaxy contribution. The solid line is the best fit to the relationship  $\log(R_{BLR}) = -21.3 + 0.519 \log(L)$ . Bottom: the Mass–Luminosity diagram. The black hole mass of the majority of AGNs was taken from Peterson et al. (2004), except for Mrk 290, Mrk 817, NGC 3227, NGC 3516, NGC 4051, and NGC 5548, for which new results by Denney et al. (2010) were used. Solid lines show the Eddington limit  $L_{Edd}$  and its 10% and 1% fractions. The position of Mrk 6 nucleus is indicated on both plots.

NGC 3516, NGC 4051, for which we used new data from Denney et al. (2010).

## 7 VELOCITY-RESOLVED REVERBERATION LAGS

### 7.1 Entire time interval: 1993–2008

The question about whether the direction of gas motion can be determined from the response of the line profile to the continuum changes was firstly raised by Fabrika (1980). Generally speaking, the BLR gas velocity field can be random circular orbits, radial gas outflow or infall, or Keplerian motion. Examples demonstrating how the velocity resolved responses can be related to different types of BLR gas kinematics are given in Peterson (2001) and Bentz et al. (2009b). The random circular orbits generate a symmetric lag profile with the highest lag observed around zero velocity. The infall kinematics produces longer lags in the blue-shifted emission,

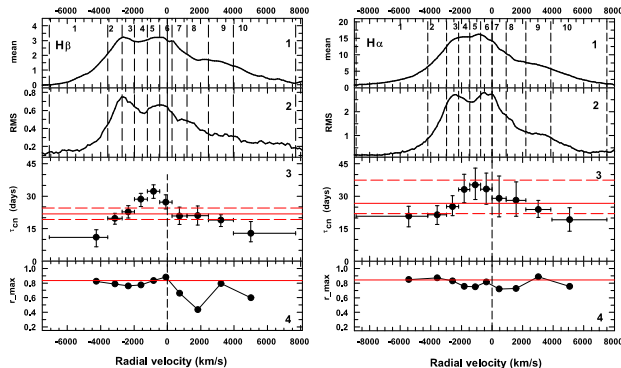


**Figure 8.** Two top panels show the  $H\beta$  mean and rms profiles (left) and the  $H\alpha$  mean profile (right) divided into ten bins of equal flux separated by vertical dashed lines. The flux units for the mean and rms profiles are  $10^{-13}$  ergs  $\text{cm}^{-2}$   $\text{s}^{-1}$   $\text{\AA}^{-1}$ . The third panels from the top show the corresponding velocity-resolved time lag response, where the delays are plotted at the flux centroid of each velocity bin. Here the vertical error bars are  $1\sigma$  uncertainties in the lag for each velocity bin denoted by the horizontal error bars. The horizontal dotted and dashed lines on the third panels mark the mean centroid lag and  $1\sigma$  uncertainty, respectively, for the entire emission line. The bottom panels show the peak value of the correlation coefficient between the bin flux in the line and continuum. Here the horizontal dotted lines mark the correlation coefficient  $r_{max}$  between the entire emission line and the continuum, as calculated in Table 5.

and the outflow gas produces longer lags in the red-shifted emission.

Horne et al. (2004) formulated some important observational requirements for determining a reliable velocity field of the BLR: (1) the time duration of observations should be at least three times larger than the longest timescale of response, (2) the mean time between subsequent observations should be at least two times less than the BLR light-crossing time, and (3) the velocity sampling  $\Delta V$  used for the velocity-delay maps should be no less than the spectral resolution of the data. According to Horne et al. (2004), such conditions can allow one to distinguish clearly between alternative kinematic models of the BLR gas motion.

In order to obtain the velocity-delay map, we measured the lag as a function of velocity in several bins across the line profile. We divided both the  $H\alpha$  and  $H\beta$  lines into ten bins of equal flux, and the width of these bins was no less than  $1000\text{--}1500$   $\text{km s}^{-1}$ . For each bin we calculated light curves from the Balmer line fluxes. Then each of these light curves was cross-correlated with the continuum light curve following the same procedure as described in Section 3. Figure 8 shows hydrogen line profiles (mean and rms) subdivided into bins (two upper panels). The two middle panels demonstrate the lag measurements for each of the bins. The vertical error bars show  $1\sigma$  uncertainties for the time lag, and the horizontal bars represent the bin width. The horizontal solid and dashed lines in the two middle panels show the mean BLR

lag and associated errors as listed in Table 5. The bottom panels show the peak correlation coefficient between the bin flux in the line and continuum,  $r_{max}$ . Figure 8 shows that

(1) The mean and rms profiles of  $H\beta$  and  $H\alpha$  are not symmetric with respect to zero velocity. The centroid of the mean and rms profiles is shifted to the short-wave part of the line. The variable parts of  $H\beta$  and  $H\alpha$  have two well-defined peaks, one of them is almost central (between 5 and 6 bins) and another is blue-shifted. In addition, there is a weaker peak in the red part of the line profile.

(2) The time delay between the higher velocity gas in the BLR and the continuum is shorter than the delay between the low velocity gas and the continuum. Such a behaviour is typical for virialized gas motions.

(3) The lag in the blue wing of the  $H\beta$  line is greater than the lag in the red side of this line. The  $H\alpha$  velocity-resolved lags shows the same tendency. This is consistent with expectations from the infall model of gas motion. Thus, it is possible we have virialized motion combined with infall signatures.

(4) The correlation coefficient of different segments of the lines is different. The bin corresponding to a radial velocity of  $V_r \approx +1500$   $\text{km s}^{-1}$  shows poor correlation with the continuum variation, especially in  $H\beta$ . This fact was earlier noted by Sergeev et al. (1999).

## 7.2 Velocity delay maps in the five time intervals

We have computed the velocity-resolved time delays for the five time intervals given in Table 6. For each subset we made the velocity-dependent cross-correlation analysis for the  $H\beta$  line profile bins as described in the previous section. The  $H\beta$  line was selected because its sampling is better. In Figure 9 the mean and rms  $H\beta$  profiles, the velocity-resolved time lag response, and the velocity-dependent peak correlation coefficient are shown for the five time intervals. Upon inspection of Figure 9 it becomes clear that the mean and rms profiles are different among the five periods. The relative intensity in the blue peak and in the central peak changes very strongly: during the first interval the blue peak is higher than the red one. The opposite situation is seen in the fifth interval. The flux in continuum as well the flux in the  $H\beta$  line systematically decreased from the second to the fourth time interval, as is seen in Figure 3 and Figure 7. The  $H\beta$  rms profile shows two peaks in the first, second and third period, the flat top in the fourth period, and in the fifth period we see three peaks.

Figure 8 demonstrates that the high-velocity gas in the wings exhibits a shorter lag than the low-velocity gas, supporting the virial nature of gas motion in BLR: the gas kinematics that is dominated by the central massive object.

However, the lag is slightly larger in the blue wing than in the red wing for all subintervals. This is a signature of the infall gas motion. In the fifth period (2005–2008) the velocity delay map is more symmetric, but the seventh bin shows very small lag, as well as in the previous time interval. For 2005–2008 there is a poor correlation with the continuum for bins 7–10. A more detailed examination of the bin light curves for 2005–2008 (Figure 10) revealed that there is a trend for the  $H\beta$  flux in bins 7–10, which is almost absent in the bins 1–6. Following the advice of our

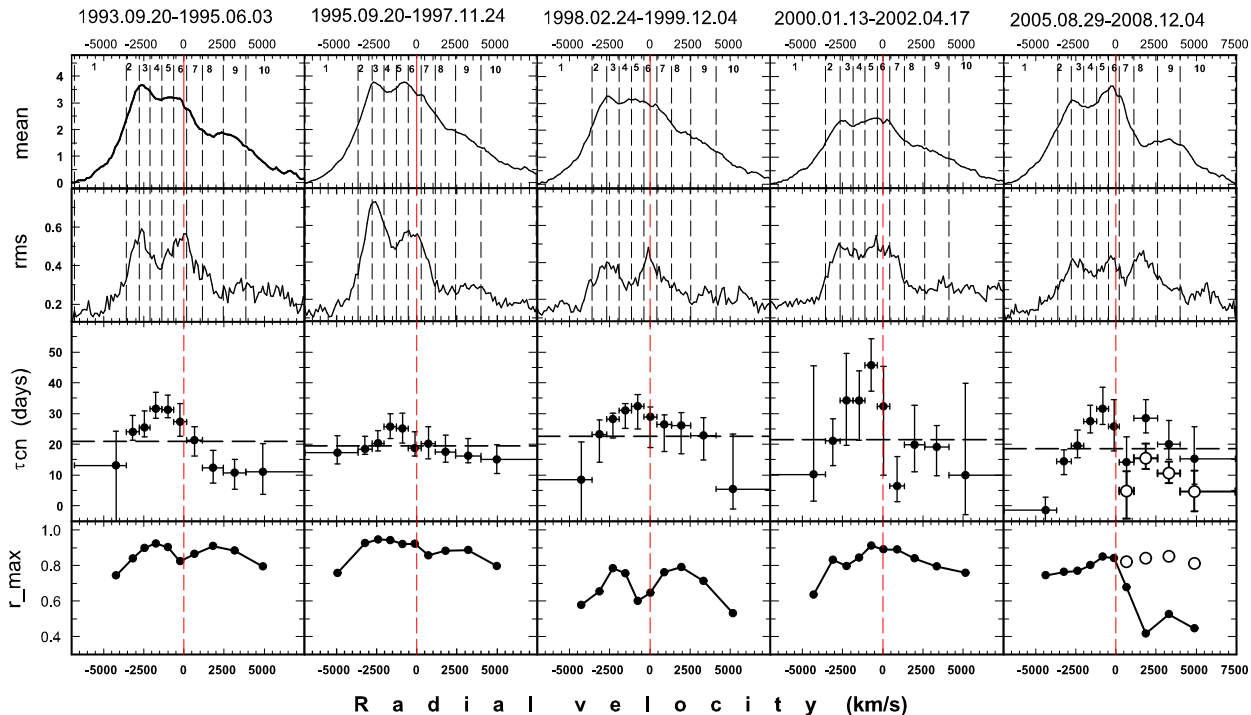


Figure 9. The same as in Figure 8, but for the  $H\beta$  line for the five time intervals.

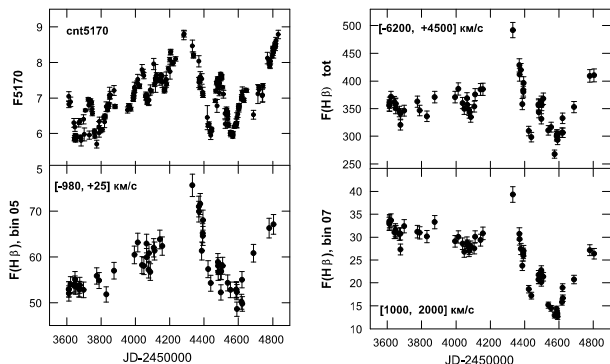


Figure 10. Light curves in the continuum and  $H\beta$  in 2005–2008 over the velocity range from  $-6200$  to  $+4500$   $\text{km s}^{-1}$  (top panels) as well as the light curves of the broad  $H\beta$  line in bin 5 in the velocity range from  $-980$  to  $+25$   $\text{km s}^{-1}$ , and in the bin 7 in the velocity range from  $1000$  to  $2000$   $\text{km s}^{-1}$  (bottom panels). The continuum fluxes are in units of  $10^{-15}$   $\text{erg s}^{-1} \text{cm}^{-2} \text{\AA}^{-1}$ , and the broad emission line fluxes are in units of  $10^{-15}$   $\text{erg s}^{-1} \text{cm}^{-2}$ .

reviewer we removed the trend from the  $H\beta$  light curves for bins 7–10. No more significant trends were found for other time intervals. In Figure 9 the detrended lags and correlation coefficients are shown by open circles. After detrending procedure, the lag–velocity dependence became more similar to the lag–velocity dependence for the first period, for which the difference in lag between the blue and red wings is largest.

So, it is most likely that the BLR kinematic in Mrk 6

is a combination of the Keplerian gas motion and infall gas motion.

## 8 CONCLUSION

We have reported our new results on the Mrk 6 nucleus from 1998–2008 observational data together with the previous results published by Sergeev et al. (1999). We found that

(1) The flux of the Mrk 6 nucleus in 1992–2008 varied significantly in the continuum as well as in the  $H\alpha$  and  $H\beta$  broad emission lines. The relative amplitude of the continuum flux variability is larger than in the hydrogen lines, and it is greater in the  $H\beta$  line than in the  $H\alpha$  (see Table 4). It is typical for the most of Seyfert galaxies. This agrees with the predictions of Korista & Goad (2004) based on new photo-ionization calculations of the BLR-like gas.

(2) We found the average time delay between the total  $H\beta$  flux and the continuum flux at  $5170$   $\text{\AA}$  to be  $21.1 \pm 1.8$  days, and the time delay does not vary significant among individual time intervals. It seems that the size of the  $H\beta$  emission region remains approximately the same over long time periods. The  $H\alpha$  flux responds to the changes in the  $F5170$  continuum with a lag of  $26.8^{+10.6}_{-4.8}$  days.

(3) When the continuum flux varies, the photo-ionization models predict the existence of the relation between the BLR size and the luminosity. However, because the large uncertainties in the lag for individual time intervals we are unable to find such a relation. For the same reason, it is unable to obtain a dependence between the lag and line width, and it is impossible to check whether this dependence is consistent

with the dependence  $V \propto r^{-1/2}$  expected for the gravitationally dominated motion.

(4) The  $H\beta$  line width is larger than that of  $H\alpha$ . This is naturally explained by photo-ionization calculations (e.g., Korista & Goad 2004): the effective emission region of  $H\beta$  is smaller and closer to the ionizing source than the effective region of  $H\alpha$ , and the gas velocities in  $H\beta$  are higher.

(5) By examining the velocity-resolved lags for the broad  $H\beta$  and  $H\alpha$  lines, we found that the lag in the high-velocity wings are shorter than in the line core. This indicates virial motions of gas in the BLR. However, the lag is slightly larger in the blue wing than in the red wing for the entire time interval as well as for the individual periods considered in the present paper. This is a signature of the infall gas motion. Probably the BLR kinematic in the Mrk 6 nucleus is a combination of the Keplerian gas motion and infall gas motion.

(6) Some profile segments often show poor correlation with the continuum flux. According to Gaskell (2010) this effect can arise because off-axis sources of ionizing continuum flux can appear, which might not make a detectable contribution to the total continuum flux variability, but they will have an influence on the line only over a narrow range of radial velocity in the BLR. If these local off-axis events will vary out of phase with the variability of the dominant source, the result will be to give a weak correlation between the continuum flux and the line flux in the narrow range of radial velocity.

(7) We determined the black hole mass from the lag and line width measurements of the  $H\beta$  and  $H\alpha$  lines. The mass was found to be  $M_{BH} = (1.8 \pm 0.2) \times 10^8 M_{\odot}$  for the  $H\beta$  line and slightly greater and less reliable from the  $H\alpha$  line. Under such a mass and the luminosity of  $\lambda L_{\lambda}(5100) = (2.51 \pm 0.38) \times 10^{43} \text{ erg s}^{-1}$ , the Mrk 6 nucleus is located on the upper edge of the Mass-Luminosity diagram that corresponds to the Eddington ratio of about 0.01. This confirms the assumption (e.g., Sergeev et al. 2011) that there is anticorrelation between broad-line widths and Eddington luminosity ratio  $L_{bol}/L_{Edd}$ . The Mrk 6 position on the BLR Size–Luminosity diagram does not contradict the fit  $R_{BLR} \propto L^{0.5}$  determined by Bentz et al. (2009a).

## ACKNOWLEDGMENTS

We thank the anonymous reviewer for useful comments and suggestions. We also thank S. Nazarov and the staff of 2.6-m and 0.7-m telescope for help during our observations. SSG acknowledges the support to CrAO in the frame of the ‘CosmoMicroPhysics’ Target Scientific Research Complex Programme of the National Academy of Sciences of Ukraine (2007–2012). VTD acknowledges the support of the Russian Foundation of Research (RFBR, project no. 09-02-01136a). The CrAO CCD cameras were purchased through the US Civilian Research and Development for Independent States of the Former Soviet Union (CRDF) awards UP1-2116 and UP1-2549-CR-03.

## REFERENCES

Bentz M.C. et al., 2008, ApJ, 689, L21  
Bentz M.C. et al., 2009a, ApJ, 697, 160

Bentz M.C. et al., 2009b, ApJ, 705, 199  
Bentz M.C. et al., 2010, ApJ, 716, 993  
Blandford R.D., McKee C.F., 1982, ApJ, 255,419  
Collin S., Kawaguchi T., Peterson B.M., Vestergaard M., 2006, A&A, 456, 75  
Denney K.D., Peterson B.M., Pogge R.W. et al., 2009, ApJ, 704, L80  
Denney K.D., Peterson B.M., Pogge R.W. et al., 2010, ApJ, 721, 715  
Doroshenko V.T., 2003, A&A, 405, 903  
Doroshenko V.T., Sergeev S.G., 2003, A&A, 405, 909  
Doroshenko V.T., Sergeev S.G., Merkulova N.I., et al., 2005, Astrophysics, 48, 156  
Fabrika S.N., 1980, Astron. Tsirk., No 1109, 1  
Feldmeier J.J. et al., 1999, ApJ, 510, 167  
Gaskell C.M., 2009, [arXiv:0910.3945]  
Gaskell C.M., 2010, [arXiv:1008.1057]  
Gaskell C.M., Sparke L.S., 1986, ApJ, 305, 175  
Graham A.W., Onken Ch.A., Athanassoula E. and Combes F. 2011, MNRAS, 412, 2211  
Horne K. et al., 2004, PASP, 116, 465  
Immler S., Brandt W.N., Vignall Cr., et al., 2006, AJ, 126, 153  
Kaspi S., Smith P.S., Netzer H. et al., 2000, ApJ, 533, 631  
Khachikian E. Ye.&Weedman D.W., 1971, ApJ, 164, L109  
Kharb P., O’Dea C.P., Baum S.A., Colbert E.J.M., Xu C., 2006, ApJ, 652, 177  
Kharitonov A.V., Tereshchenko V.M., Knyazeva L.N., 1988, Spectrophotometric Catalogue of Stars, Science, Moscow: Nauka  
Koratkar A.P., Gaskell C.M., 1991, ApJS, 75, 719  
Korista K.T., Goad M.R., 2004, ApJ, 606, 749  
Kukula M.J., Holloway A.J., Pedlar A., et al., 1996, MNRAS, 280, 1283  
Malizia A. Bassani L., Capalbi M., et al., 2003, A&A, 406, 105  
Marconi A., Axon D.J., Vaiolino R. et al., 2008, ApJ, 678, 693  
Marconi A., Axon D.J., Vaiolino R. et al., 2009, ApJ, 698, L103  
Neizvestny S.I., 1987, Izv.SAO, 24, 3  
Netzer H., 2009, ApJ, 695, 793  
Onken C.A., Ferrarese L., Merritt D. et al., 2004, ApJ 615, 645  
Peterson B.M., 1988, PASP 100, 18  
Peterson B.M., 2001, [arXiv: astro-ph/0109495]  
Peterson B.M., Ferrarese L., Gilbert K.M. et al., 2004, ApJ, 613, 682  
Peterson B.M., Wanders I., Horne K., et al., 1998, PASP 110, 660  
Schlegel D.J., Finkbeiner D.P., Davis M., 1998, ApJ, 500, 525  
Schurch N.J., Griffiths R.E., Warwick R.S., 2006, MNRAS, 371, 211  
Sergeev S.G., Pronik V.I., Sergeeva E.A. Malkov Yu.F., 1999, ApJS, 121, 159  
Sergeev S.G., Doroshenko V.T., Golubinskiy Yu.V., et al., 2005, ApJ, 622, 129  
Sergeev S.G., Klimanov S.A., Doroshenko V.T. et al., 2011, MNRAS, 410, 1877  
Wandel A., Peterson B.M., Malkan M.A., 1999, ApJ, 526, 579



- Wanders I. & Peterson B.M., 1996, ApJ, 466, 174  
Welsh W.F., 1999, PASP, 111, 1347  
White R.J., Peterson B.M., 1994, PASP, 106, 879  
Woo J.-H., Treu T., Barth A.J. et al., 2010, ApJ, 716, 269